Fuel Processing Technology 291 (2026) 108554

Contents lists available at ScienceDirect

Fuel Processing Technology

journal homepage: www.elsevier.com/locate/fuproc

Thermo-catalytic conversion of actual drax biomass combustion residue into porous carbon: A dual valorisation approach

Kofoworola Awodun, Yinghe He, Salman Masoudi Soltani *

Department of Engineering, Brunel University of London, Uxbridge UB8 3PH, UK

ARTICLE INFO

Keywords:
Biomass
Pyrolysis
Activation
Adsorbent

ABSTRACT

The valorisation of combustion residues offers a sustainable route to support sustained development of biomass power plants. This study investigates the synthesis of Ca-enhanced porous carbons from biomass combustion residues sourced from Drax Power Station (UK) and post-consumer chicken eggshells. Unburnt biomass was selectively recovered through systematic drying, size fractionation, and ultrasonic treatment, producing a carbon-rich precursor with reduced inorganic contamination. The recovered biomass was systematically pyrolysed, Ca-enhanced, and activated to yield a structurally stable porous sorbent with a fixed carbon content of 61%. Raman analysis confirmed turbostratic carbon formation with consistent defect characteristics (ID/IG ≈ 0.65), while FTIR spectra showed substantial attenuation of lignocellulosic O—H and C═O functionalities following carbonisation. Surface enhancement was achieved via eggshell-assisted calcium incorporation through dry-mixing and Ca-ion impregnation, with the latter producing superior dispersion and controlled pore development. Subsequent physical activation demonstrated that CO_2 activation outperformed steam activation, generating predominantly microporous carbons with a total accessible surface area of 463 $m^2\ g^{-1}$, micropore surface area of 384 $m^2\ g^{-1}$ and an estimated external surface area of 92 $m^2\ g^{-1}$. The resulting surface area was comparable to those reported for several physically activated biomass-derived carbons while avoiding chemical activating agents.

1. Introduction

The development of functional porous materials has become a central research focus across environmental, chemical, and energy-related disciplines due to their ability to provide high interfacial surface area, tuneable pore structures, and chemically active surfaces. These properties make porous solids attractive for a broad range of applications, including gas storage and separation, catalysis, pollutant removal, energy storage, and advanced adsorption-based purification processes [1,2]. In particular, the performance of porous materials is strongly governed by three key design features: (i) high accessible surface area, (ii) pore size distribution tailored to the target molecule or ion, and (iii) surface chemistry capable of enhancing specific interactions through polarity, acid-base affinity, or catalytic activity [3,4]. Achieving an optimal balance of these structural and chemical characteristics remains a major challenge, particularly when scalability and cost-effectiveness are considered.

A wide variety of porous materials have been explored in the literature, including activated carbons, zeolites, mesoporous silicas, covalent organic frameworks (COFs), and metal-organic frameworks (MOFs) [5–8]. Although MOFs and COFs exhibit exceptional structural tunability and high theoretical surface areas, their synthesis often requires high-purity precursors, complex processing routes, and controlled operating conditions, which can limit scalability and increase economic and environmental burdens [9]. Zeolites and ordered mesoporous silicas, while widely used in adsorption and catalysis, are similarly

Abbreviations: ASTM, American society for testing and materials; BBD, Box-Behnken design; BCBA, biomass combustion bottom ash; BET, Brunauer-Emmett-Teller; CaA, calcium acetate; CCD, central composite design; COFs, covalent organic frameworks; CrI, crystallinity index; DoE, design of experiments; EDS, energy-dispersive X-ray spectroscopy; ESP, eggshell powder; FC, fixed carbon; FTIR, Fourier-transform infrared; ICDD, International Centre for Diffraction Data; MOFs, metal-organic frameworks; NLDFT, non-local density functional theory; OFAT, one factor at a time; SEM, scanning electron microscope; SEM-EDS, scanning electron microscope with energy-dispersive X-ray spectroscopy; TGA, thermogravimetric analysis; uB, unburnt biomass; VOM, volatile organic matter; XRD, X-ray diffractometer/X-ray diffraction.

* Corresponding author.
E-mail address: Salman.MasoudiSoltani@brunel.ac.uk (S. Masoudi Soltani).

https://doi.org/10.1016/j.fuproc.2026.108554
Received 16 June 2026; Received in revised form 28 July 2026; Accepted 29 July 2026
Available online 31 July 2026

constrained by the need for controlled synthesis environments and, in many cases, structure-directing agents that raise production costs and contribute to chemical waste generation [10,11]. In contrast, activated carbons remain among the most versatile and industrially established porous materials due to their thermal stability, chemical resistance, broad precursor availability, and the ability to engineer their pore structure and surface chemistry through relatively simple thermal and activation processes. Furthermore, their performance can be significantly enhanced by surface functionalisation or mineral modification, introducing basic sites or oxygenated groups that strengthen interactions with CO_2 [4]. Their adaptability has positioned activated carbons as leading candidates for scalable porous material production, particularly when derived from renewable or waste-based feedstocks. Specifically, biochar, a carbon-rich material produced through the thermochemical conversion of biomass under oxygen-limited conditions, has attracted increasing attention as a versatile platform for environmental and energy applications. Recent advances have demonstrated that engineered biochars, through controlled modification of their surface chemistry, porosity, and mineral composition, can be tailored for applications including pollutant removal, carbon capture, catalysis, and energy storage [12–15]. The intrinsic tunability of biochar properties, which depends on feedstock characteristics and thermal conversion conditions, provides opportunities for transforming low-value biomass residues into functional carbon materials for sustainable technologies.

The increasing demand for sustainable porous materials has accelerated interest in waste-to-resource strategies, where carbonaceous and mineral-rich residues are repurposed as precursors for functional adsorbents and catalysts. Such approaches are aligned with circular economy principles, aiming to reduce dependence on virgin raw materials while simultaneously mitigating the environmental impacts associated with waste disposal [16,17]. Among emerging waste-derived resources, biomass combustion residues have gained significant attention due to the rapid global expansion of biomass utilisation for renewable energy generation. Large-scale biomass combustion is now widely deployed as part of decarbonisation strategies in power generation, yet it produces substantial quantities of solid by-products, particularly fly ash and bottom ash, which remain underutilised in many regions.

Drax Power Station in Selby, United Kingdom, represents a prominent example of this challenge. As the world's largest dedicated biomass-fired thermal power plant, with an estimated generation capacity of approximately 3.2 GW, Drax supplies around 8% of the UK's electricity demand [18]. To meet this electricity demand, Drax consumes close to 9 million tonnes of compressed wood pellets annually, primarily sourced from forestry residues and energy crops [19]. While the conversion of Drax from coal to biomass in 2013 has contributed significantly to renewable electricity generation, the combustion process generates large volumes of ash residues. Biomass combustion bottom ash (hereafter referred to as BCBA) has been found in this research to be a particularly complex and heterogeneous material, comprising mineral oxides, alkali and alkaline earth metals (e.g., K, Ca, Mg), partially combusted organics, and unburnt lignocellulosic biomass fragments. This compositional complexity, coupled with variability in feedstock and combustion conditions, often limits its direct reuse and leads to stockpiling or disposal and comes with associated economic and environmental costs. Consequently, the development of strategies capable of selectively recovering the residual carbon fraction and upgrading BCBA into value-added porous materials represents a promising pathway for improving industrial resource efficiency.

In parallel, the agricultural and food processing industries generate substantial quantities of calcium-rich biogenic waste, among which chicken eggshells are particularly abundant. Global egg production exceeds 80 million tonnes annually, producing an estimated 8–10 million tonnes of eggshell waste each year [20]. Large-scale egg processing facilities, which manufacture liquid or powdered egg products, generate concentrated eggshell waste streams that are commonly disposed of through landfilling or incineration, contributing to environmental burdens such as odour generation and microbial contamination due to residual organic membranes [21]. Chemically, eggshells are composed primarily of calcium carbonate (typically 94–97 wt%), with minor amounts of magnesium carbonate, calcium phosphate, and organic proteinaceous membranes [22]. This high $CaCO_3$ content makes eggshells a renewable and widely available alkaline resource, with potential applications in catalysis, bio-ceramics, adsorbent synthesis, soil amendment, and materials engineering. Despite extensive laboratory-scale studies, large-scale valorisation of eggshell waste remains limited, leaving a significant opportunity for industrially relevant circular utilisation [23,24]. In the context of rising demand for sustainable and low-cost materials, eggshell presents an attractive feedstock for circular materials engineering, offering opportunities to simultaneously address waste management challenges and enhance the functionality of porous materials for environmental applications.

The co-utilisation of BCBA and eggshell waste presents an attractive and underexplored pathway for porous carbon engineering. BCBA provides a partially thermally processed, carbon-containing feedstock, potentially reducing energy demand during carbonisation while retaining reactive lignocellulosic structures. Eggshell-derived calcium carbonate can act as a mineral modifier and catalytic agent, influencing pyrolysis and activation behaviour. During high-temperature treatment, $CaCO_3$ decomposes into CaO with the release of CO_2, which may promote pore evolution and enhance carbon reactivity, particularly during subsequent physical activation stages [25]. Furthermore, calcium species are known to catalyse carbon gasification reactions, enabling controlled pore development and improving microporosity under appropriate process conditions. When combined, these two waste streams offer a route toward in-situ mineral-assisted carbonisation and activation, reducing reliance on conventional chemical activating agents such as KOH, $ZnCl_2$, or H_3PO_4, which are effective but often associated with corrosive processing conditions, extensive washing requirements, and secondary wastewater generation [26]. Therefore, the integration of waste-derived calcium with carbon-rich industrial residues offers a chemically benign approach for producing tunable porous materials.

1.1. Motivation, aim & objectives

The transformation of industrial residues and agricultural by-products into functional porous materials directly supports the principles of sustainable materials engineering and circular economy development. BCBA represents an underutilised waste stream containing a residual carbon fraction, while post-consumer eggshell waste provides an abundant calcium-rich resource. Integrating both waste streams offers a unique opportunity to develop low-cost porous materials through synergistic mineral-carbon interactions, potentially enhancing pore development and surface functionality without the need for aggressive chemical activation. Beyond waste mitigation, this approach addresses the growing demand for scalable porous solids in adsorption and purification technologies, positioning waste-derived porous carbon as a practical and sustainable alternative to conventional high-cost porous material synthesis routes. Additionally, incorporating calcium-based compounds during the synthesis of porous materials can promote pore development through pore-forming and/or hard-templating effects, applicable to both carbonaceous [27–29] and non-carbon porous frameworks [30,31]. Therefore, in-situ catalytic pyrolysis of recovered biomass from BCBA using calcium derived from eggshells has potential to form porous carbon materials.

Over the past two decades (Fig. 1), research activity in biomass-derived porous materials has expanded significantly, driven by increasing global demand for sustainable solutions in environmental remediation, catalysis, and separation science. Researchers have found that alkaline-earth metals like calcium can be useful in improving carbon materials during synthesis [32–35]. However, despite the

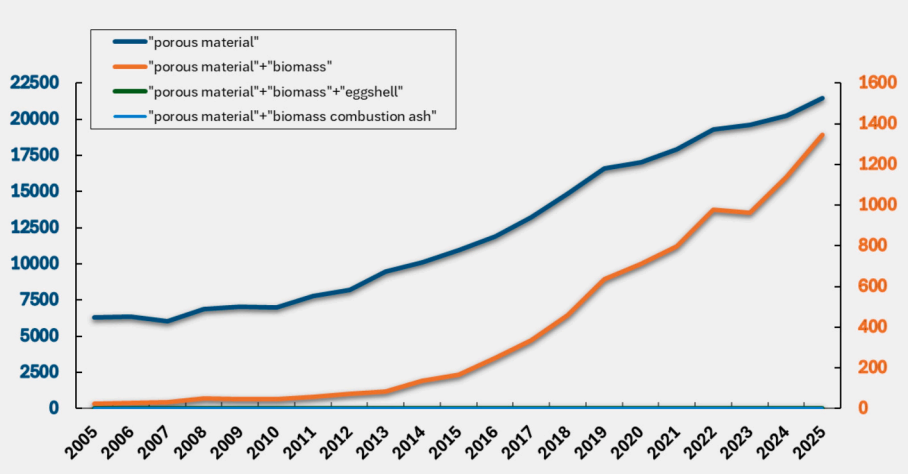

Fig. 1. Scopus-indexed publications from 2005 to 2025.

demonstrated catalytic and structural benefits of calcium-based modifiers in carbon synthesis, the integration of waste eggshells with biomass-derived carbon systems remains relatively limited (Fig. 1). Research specifically combining biomass combustion residues such as BCBA with eggshell-derived calcium sources remains scarce. This gap highlights an important opportunity to explore synergistic dual-waste systems for engineered porous materials that simultaneously address waste management challenges and the demand for sustainable adsorbents.

Therefore, the aim of this research was to investigate the feasibility of thermo-chemical conversion of BCBA generated at Drax power plant and post-consumer eggshell waste into functional porous adsorbents suitable for other applications through controlled pyrolysis, and surface modification. The specific objectives considered to achieve this aim were to:

1. Evaluate the suitability of BCBA as a carbon precursor by investigating its thermal conversion behaviour and optimising pyrolysis conditions to promote the formation of a stable carbon matrix.
2. Investigate the effect of eggshell-derived calcium species on surface development of BCBA during thermal conversion, through dry-mixing and calcium-ion impregnation approaches, to enhance pore formation and structural evolution of the carbon material.
3. Investigate the effect of physical activation on the eggshell-modified char using CO_2 and steam.
4. Characterise the structural, chemical, and adsorption properties of the synthesised materials, using complementary techniques to establish relationships between synthesis conditions and pore development.

2. Materials and methods

A structured and statistically guided experimental methodology was adopted to synthesise and evaluate porous carbon adsorbents. This involved precursor preparation, controlled pyrolysis, eggshell-assisted surface modification, porosity enhancement with subsequent material characterisation to investigate porosity performance Fig. 2. Detailed experimental procedures were implemented using multiple design of experiments (DoE) frameworks, including full factorial, central composite (CCD), and Box-Behnken (BBD) designs, to systematically evaluate the effects and interactions of key processing variables. The specific design structures and associated experimental procedures are described in the relevant subsections.

2.1. Materials

The materials used in this study included biomass combustion bottom ash (BCBA) from Drax Power Station, Selby, UK, and post-consumer chicken eggshells collected locally from Lancaster Hotel, Brunel University of London, UK. Chemical reagents and gases used included acetic acid (CH_3COOH, ≥ 99.7%, Fisher Scientific, UK), nitrogen (N_2, 99.999%, BOC, UK), carbon dioxide (CO_2, 99.995%, BOC, UK), and Helium (He, 99.999%, BOC, UK). Deionised water was prepared using Suez Analyst 160 GP water purification system (resistivity ≥18.2 MΩ·cm). All chemicals and gases were used as received without further purification.

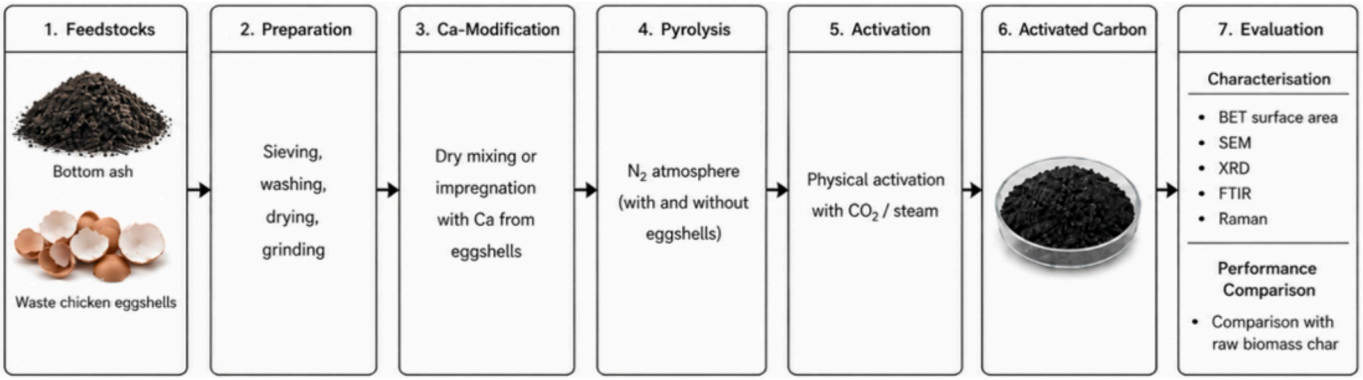

Fig. 2. Breakdown of experimental methodology.

2.2. Precursor preparation

2.2.1. Extraction of biomass from bottom ash

The as-received BCBA was manually mixed thoroughly to ensure homogeneity within the bulk waste residue. The BCBA was then spread evenly in stainless steel trays (approximately 500 g per tray) and dried in a convection oven at 100 °C for 24 h to remove residual moisture. After drying, the BCBA was subjected to size separation using a combination of mechanical ball milling and sieving techniques. The entire contents of the tray, now filled with dry BCBA, was placed in a 5 L ball-mill jar and milled using the Capco Ball Mill Model 2, at a speed of 150 rpm for 1 h. After ball milling, the content of the jar was transferred to a series of sieves, ranging from 0.4 to 2.0 mm, and placed on a Retsch vibratory sieve shaker (AS 200 basic) at 30 Å for 30 min. This procedure enabled selective separation of unburnt biomass-rich fractions based on particle size. The coarser fractions (1.4–2.0 mm), visually enriched in fibrous and woody material, were collected and designated as the unburnt biomass fraction for further processing, while finer, mineral-dominated fractions were excluded from this study. This fraction, for the purpose of this research has been called unburnt biomass (referred to as uB hereafter).

To reduce surface-bound inorganic ash, the collected unburnt biomass fractions were subjected to ultrasonic washing in deionised water. The ultra-sonication experiments were carried out using a randomised 3 × 3 full factorial screening design (factors: solid-to-liquid ratio, amplitude and time). Briefly, 20 g of uB was placed in a glass beaker and mixed with distilled water at a set solid-to-liquid ratio (*w/v*). Ultrasonication was carried out using a Fisher Scientific Sonic Dismembrator (500 W) equipped with a 250 ml probe tip. The probe was immersed in the beaker (not exceeding the manufacturer's probe limit), and the suspension was sonicated at a set amplitude for a given amount of time within a sonication enclosure. Once the sonication time elapsed, the liquid phase was manually decanted by carefully tilting the beaker to remove suspended ash particles. The washed uB was collected and oven-dried at 100 °C for 24 h. This sonication-washing procedure was repeated for all experiments and statistically analysed using Minitab software. Ash mass was used as the selected response, and this was quantified by combustion of the washed uB using the standard test method for ash in wood (ASTM D1102–84) [36]. The calculated ash content was identified as the total ash content of the sample (including surface and bulk ash). The best conditions were selected (for minimisation of ash mass), the procedure repeated for validation and the resulting sonicated samples (denoted as uB_S hereafter) stored in airtight containers for further processing.

2.2.2. Preparation of waste chicken eggshells

The collected eggshells were thoroughly rinsed with deionised water to remove residual albumen and loosely attached membrane material. Eggshells with persistent inner membranes were subsequently placed in an ultrasonic bath filled with deionised water and sonicated for 1 h to facilitate complete membrane removal. The cleaned eggshells were then removed and air-dried for approximately 4 h. Dried eggshells were manually crushed and ground using a ceramic mortar and pestle to obtain fine powder. The resulting material was passed through a 250 μm sieve to ensure a uniform particle size fraction (< 250 μm). The eggshell powder (ESP, hereafter) was collected and stored in airtight containers for subsequent use.

A specific amount of the obtained ESP was directly used for dry-mixing experiments. However, for calcium ion extraction (for impregnation experiments), the ESP was dissolved in 1.5 M acetic acid. The stoichiometry of the dissolution reaction (Eq. (1)) was used to calculate the quantity of eggshell that would completely dissolve in 100 ml of 1.5 M acetic acid. In each batch, 7.5 g of ESP was placed in a glass beaker, followed by the addition of 100 ml of 1.5 M acetic acid under continuous stirring at 300 rpm using a magnetic stirrer. The reaction was conducted at a constant temperature of 20 °C. The pH of the suspension was continuously monitored using an Oakton pH 700 benchtop pH meter. Stirring was maintained until the pH remained stable for at least 1 h, indicating completion of calcium carbonate dissolution. The resulting calcium-acetate solution was filtered to remove insoluble residues and used immediately for impregnation experiments.

$$CaCO_{3(s)} + 2CH_3COOH_{(aq)} \rightarrow Ca(CH_3COO)_{2(aq)} + H_2O_{(l)} + CO_{2(g)} \quad (1)$$

2.3. Pyrolysis of eggshell-free biomass

The sonicated biomass uB_S was subjected to pyrolysis in a tubular furnace under an inert nitrogen atmosphere, without the addition of eggshells, to produce a baseline carbon material. For each experiment, 20 g of uB_S was placed in a ceramic crucible and heated from ambient temperature to the target pyrolysis temperature (400–800 °C) at a controlled heating rate (5–15 °C min^{-1}). The final temperature was maintained for a residence time of 30–90 min to ensure complete carbonisation. Throughout the process, a constant nitrogen flow rate of 150 ml min^{-1} was applied to prevent oxidative degradation. Upon completion of pyrolysis, the furnace was allowed to cool naturally to room temperature under continuous nitrogen flow. The resulting baseline char was collected, gently ground using a mortar and pestle, and stored in airtight containers prior to subsequent surface modification and characterisation.

Eggshell-free pyrolysis experiments were designed and analysed using a randomised dual-response face-centred CCD incorporating three independent factors: pyrolysis temperature, heating rate, and hold time. The experimental matrix comprised eight cube points, six axial points, and six centre points, resulting in a total of 20 experimental runs. Char yield and fixed carbon (FC) content were selected as the response variables. Char yield was determined gravimetrically using an analytical balance and reported as a percentage of the initial biomass mass. FC content was quantified using a thermogravimetric analyser (TGA) Mettler Toledo TGA2. All experimental runs were conducted following the same pyrolysis protocol described above. Statistical analysis, response surface modelling, and dual-response optimisation were performed using Minitab software, and the predicted optimal conditions were subsequently validated experimentally using identical procedures. The char obtained from the validated optimal conditions was collected in airtight containers and labelled C_{val}. Bulk amounts were produced following the same procedure (in batches) for further processing.

2.4. Surface enhancement of biomass using waste chicken eggshells

To modify the surface chemistry and pore structure of the uB_S, waste chicken eggshells were employed as a calcium-rich functional additive using two distinct surface enhancement strategies. These approaches were designed to introduce alkaline earth metal species and oxygen-containing surface functionalities through either physical contact or chemical impregnation, enabling comparative evaluation of their effects on carbon structure and adsorption performance. The two modification routes comprised (i) dry mixing of uB_S with ESP prior to pyrolysis and (ii) impregnation of uB_S with calcium acetate extracted from solubilised eggshells.

2.4.1. Dry-mixing biomass with eggshells

For modification via solid-state mixing, uB_S was dry mixed with ESP prior to pyrolysis. Predetermined masses of uB_S and ESP, corresponding to selected eggshell-to-biomass (ESP/uB_S) mass ratios (and a total batch mass of 20 g), were combined and manually homogenised. This was done to ensure uniform dispersion of the calcium carbonate particles throughout the biomass matrix. A single-factor (one-factor-at-a-time/OFAT), multi-response experimental design was employed, in which the ESP/uB_S ratio was systematically varied across five levels (0.05–0.25) with FC content and Brunauer-Emmett-Teller (BET) surface area as the response variables.

The homogenised mixtures were subsequently transferred to ceramic crucibles and subjected to pyrolysis under an inert nitrogen atmosphere following the same heating programme and operational conditions (as conducted for C_{val}) described in Section 2.3. After pyrolysis and natural cooling under nitrogen, the resulting eggshell-modified carbons were gently ground and stored in airtight containers for further characterisation. These samples are hereafter referred to as dry-mixed eggshell-modified carbons (C_{DM}).

2.4.2. Impregnation of biomass with calcium ions from eggshells

Modification via solution-phase ion exchange was achieved by impregnating uB_S with prepared calcium acetate solution (as described in Section 2.2.2). The experimental matrix used for this section comprised a 2 × 3 full factorial design with 2 factors (calcium acetate-to-biomass ratio and dosing time) and was response optimised for FC content and CO_2 uptake. Predetermined masses of uB_S and corresponding volumes of calcium acetate, calculated to achieve selected calcium acetate-biomass (CaA/uB_S) ratios and a total batch mass of 20 g, were combined. The resulting mixtures were agitated using a Fisher Scientific multi-platform shaker at 350 rpm for 30 min to promote uniform calcium ion diffusion and adsorption onto the biomass surface. The mixture was then placed in an oven to dry at 60 °C for 12 h. The dried, calcium-impregnated biomass was then subjected to pyrolysis under nitrogen using the same conditions (as conducted for C_{val}) outlined in Section 2.3. Upon completion of pyrolysis and cooling under inert atmosphere, the resulting impregnated carbons were recovered, gently ground manually, and stored in airtight containers for subsequent characterisation. These samples are hereafter, referred to as calcium-impregnated eggshell-modified carbons (C_{IM}).

2.5. Porosity improvement of optimum sample via physical activation

Based on the outcomes of the experimental design and preliminary characterisation, the optimum eggshell-modified carbon sample (labelled C_{opt}) was selected for further porosity enhancement via physical activation. Activation was performed using a controlled oxidising atmosphere (steam vs carbon dioxide) to promote pore development while minimising excessive carbon burn-off.

A specific quantity (5 g) of C_{opt} was placed in a ceramic crucible and heated in a Carbolite Gero TF1–1200 tubular furnace under a flowing activating agent at a predefined activation temperature, time and heating rate. Following activation, the furnace was cooled naturally to room temperature with the activating agent (except with steam which was turned off when furnace cooled to 150 °C. The activated carbon was subsequently collected, labelled and stored in airtight containers prior to further characterisation and adsorption testing. This activation step was designed to enhance accessible surface area and pore connectivity while preserving surface functionalities introduced by eggshell-derived calcium species.

For CO_2 activation, carbon dioxide was introduced in combination with nitrogen (as an inert diluent) to regulate the reactivity of the activating agent, enhance heat and mass transfer within the carbon matrix, and reduce overall process costs. The gasification of carbon by CO_2 (Eq. (2) - Boudouard reaction) proceeds via a heterogeneous surface reaction mechanism that is commonly described by a Langmuir-Hinshelwood (L-H) rate expression [37] where r is the rate of carbon gasificarion, k is the intrinsic kinetic rate constant, P is the partial pressure of different species in the gas phase and K is the adsorption equilibrium constant of the different species on active sites. In this expression (Eq. (3)), the reaction rate depends on the adsorption of CO_2 on active carbon sites and is influenced by competing surface coverage effects of product gases such as CO.

$$C_{(s)} + CO_{2(g)} \rightarrow 2CO_{(g)} \ (\Delta H > 0) \tag{2}$$

$$r = \frac{kP_{CO_2}}{1 + K_{CO_2}P_{CO_2} + K_{CO}P_{CO}} \tag{3}$$

Accordingly, the reaction rate is strongly dependent on the partial pressure of CO_2 at the carbon surface [37]. Dilution of CO_2 with an inert gas such as N_2 lowers the effective CO_2 partial pressure in the reactor atmosphere, thereby decreasing the surface coverage of CO_2 and lowering the overall gasification rate under otherwise identical conditions [38]. This controlled reduction in reactivity is beneficial for preventing excessive burn-off and enabling more uniform pore development during activation. A randomised BBD experimental design was used to investigate the effects of activation temperature, activation time and CO_2 concentration in a 200 ml/min CO_2/N_2 mixture on CO_2 adsorption. Three distinct levels for each factor (activation temperature: 750–950, activation time: 30–90 min and CO_2 concentration: 50–100%) were observed and a total of 15 experiments conducted. CO_2 uptake was the selected response, quantified using a Mettler Toledo TGA2. The experimental data was then statistically analysed and response optimised. The identified optimum was then validated under the same conditions and the resulting activated carbon labelled (AC_{CO2}).

For steam activation, a Cellkraft precision steam generator Model E-1500 (with in-built precision pump and evaporator) was attached to the tube furnace for the introduction of steam using a jacketed heating line that comes with the equipment. The steam temperature used for the activation was 150 °C. After activation, the furnace was initially allowed to cool naturally to the steam temperature, then the steam generator was turned off to introduce nitrogen during the final cool down stage to room temperature. This was done to ensure no moisture was left within the pores of the activated carbon and to ensure no condensation occurred. The reaction involved in steam activation (otherwise known as steam gasification) has been detailed in Eq. (4). A randomised BBD experimental design (like the one for CO_2 activation) was used to investigate the effects of activation temperature, activation time and steam flow on CO_2 adsorption. Three distinct levels for each factor (same as CO_2 action but replacing CO_2 concentration with steam flow: 0.5–1.5 g min^{-1}) were observed and a total of 15 experiments conducted with CO_2 uptake as response. The experimental data was then statistically analysed and response optimised. The identified optimum was then validated under the same conditions and the resulting activated carbon labelled (AC_{steam}).

$$C_{(s)} + H_2O_{(g)} \rightarrow CO_{(g)} + H_{2(g)} \ (\Delta H \backsimeq +131 \ kJmol^{-1}) \tag{4}$$

2.6. Material characterisation & analysis

The physiochemical, structural, and morphological properties of the synthesised carbon materials were systematically characterised using a suite of complementary analytical techniques. Proximate analysis was carried out using a Mettler Toledo TGA2 to determine FC and ash contents. The method used for proximate analysis for all samples included three steps: drying under 50 ml/min nitrogen from room temperature to 150 °C and held for 10 min, decomposition in inert atmosphere (N_2) by heating to 950 °C, holding for 1 h then cooling to 600 °C, and finally combustion by heating in air (50 ml/min) to 950 °C for 1 h. The proximate analysis heating rate used for all steps was 10 °C min^{-1}. The same TGA equipment was also used to measure CO_2 uptake: first degassing under nitrogen from room temperature to 150 °C, then cooling back to room temperature and introducing 50 ml/min CO_2 at room temperature (20 °C) for 1 h, when sample mass stabilised (i.e. reached equilibrium/saturation). For this paper, CO_2 uptake measured by TGA was selected as a convenient and sensitive probe molecule to evaluate accessible porosity, surface reactivity, and adsorption performance under controlled conditions. As a well-characterised adsorbate with strong affinity to microporous structures, CO_2 provides a rapid comparative indicator of pore development and adsorption capacity, making it suitable for benchmarking the effectiveness of the porosity-enhancement

strategy beyond carbon capture applications. Ultimate analysis was conducted to determine the composition of carbon, hydrogen, nitrogen and sulphur in carbon samples. It is noteworthy that although proximate and ultimate analyses give values for carbon, FC recorded in proximate analysis reflects the non-volatile combustible fraction remaining after devolatilisation while ultimate analysis records the actual percentage of carbon atoms present in the sample. FC in proximate analysis is calculated by difference and therefore, includes oxygenated structures and non-volatile inorganic-bound carbon, leading to slightly higher values compared to elemental carbon measured by ultimate analysis.

Textural properties, including specific total accessible surface area (also known as BET surface area), external surface area, micropore surface area, pore volume, and pore size distribution, were comparatively determined via N_2 (at 77 K) and CO_2 (at 273 K) [39] adsorption-desorption isotherms, measured using an Anton Paar Nova 600 physisorption analyser. Where necessary, external surface area (representing the surface associated with mesopores and the outer particle surface, excluding micropores) was identified using the t-plot method on the N_2 adsorption isotherm. Prior to physisorption analysis, samples were degassed under vacuum at elevated temperature (250 °C) with a heating rate of 25 °C min^{-1}, and a hold time of 4 h to remove adsorbed moisture and other entrapments. This was the degassing condition for all samples except for the uB_s sample which was degassed at 150 °C at the same heating rate and hold time. The relatively lower temperature ensured no decomposition of hemicellulose (which typically occurs between 250 and 350 °C [40]) during degassing. Helium has been selected to determine the free space (dead volume) of the sample cell before analysis because it is essentially non-adsorbing. This ensures accurate calculation of the amount of adsorbate gas adsorbed and hence surface area. Total accessible surface area, total pore volume and N_2- non-local density functional theory (NLDFT) pore size distributions were determined from the N_2 adsorption isotherms. On the other hand, Micropore surface area (using NLDFT theory), micropore volume and CO_2-NLDFT pore size distribution were derived from the CO_2 adsorption isotherms.

Surface morphology and elemental composition were examined using a JEOL IT200 scanning electron microscope equipped with energy-dispersive X-ray spectroscopy (SEM–EDS). Samples were mounted on aluminium stubs using conductive cupper tape and sputter coated with ultra-thin (~5 nm) layer of gold to minimise charging effects. To ensure accuracy in EDS compositions, at least three sites on each sample was analysed at 15 kV and the average value recorded. Since the carbon peak usually occurs close to the background region of the EDS spectrum, it is difficult to distinguish accurately the peak from noise and other signals, therefore EDS analysis cannot be relied on for quantification of carbon. More accurate carbon quantification was done using proximate and ultimate analyses. Crystalline phases were identified using a Rigaku Oxford single crystal X-ray diffractometer (XRD) with Cu Kα radiation over an appropriate 2θ range. Surface functional groups and chemical bonding environments were analysed by attenuated Fourier-transform infrared spectroscopy (FTIR) using a Shimadzu IRSpirit spectrometer. Raman spectroscopy was performed using a Renishaw inVia Raman microscope to evaluate the degree of carbon ordering and structural defects through analysis of the characteristic D and G bands. Collectively, these techniques enabled comprehensive assessment of the influence of eggshell-based modification, activation, and processing conditions on carbon structure and surface chemistry.

3. Results and discussions

3.1. Preparation of biomass precursor

3.1.1. Drying & size separation

Drying of the as-received BCBA was effective, with an average moisture content of 55.22% determined (Table S1 in supplementary information A). Following drying, subjecting the BCBA to ball milling and sequential sieving enabled selective isolation of unburnt biomass-rich fractions. This size separation step effectively concentrated the organic component of the residue, yielding a more homogeneous biomass precursor suitable for pyrolysis. Coarser particle fractions in the size range 0.71–2.0 mm were visually enriched in fibrous, woody material, whereas finer fractions were predominantly mineral-dominated and were therefore, excluded from further processing. Among the coarse fractions, particles in the 1.4–2.0 mm size range (uB) were selected for detailed analysis, as they contained the highest proportion of unburnt organic material, with an average yield of 37.91% (Table S2 in supplementary information A). Although not used in this study, intermediate fractions (1.0–1.40 mm) also exhibited appreciable organic content and remain viable candidates for future valorisation. Overall, the combined drying and size-separation strategy proved effective in enriching the organic fraction of BCBA, producing a reproducible and well-defined biomass precursor that underpins consistent carbonisation and subsequent surface functionalisation.

3.1.2. Optimisation of ash removal via ultra-sonication

Surface ash removal of uB was systematically investigated using a 3 × 3 full factorial screening design, in which the effects of solid-to-liquid ratio (i.e. 1/5, 1/10, and 1/15 *w/v*), ultrasonic amplitude (i.e. 25, 50, and 75%), and sonication time (i.e. 1, 3, and 5 min) were evaluated. Ash was quantified using ASTM standard test method for ash in wood (ASTM D1102–84) [36], with ash mass used as the primary response variable. The ash content and removal efficiency were calculated using Eq. (5) and Eq. (6) respectively. Across the experimental domain, ash contents ranged from approximately 1.23 to 2.26 wt% (full design provided in Table S3 in supplementary information A), indicating that ultrasonication was effective in reducing residual surface ash relative to untreated material (Table 1).

$$Ash\ content\ (\%) = \frac{mean\ ash\ mass}{sample\ mass} \times 100 \tag{5}$$

$$Ash\ removal\ efficiency\ (\%) = \frac{mean\ ash\ in\ (raw\ BCBA - method)}{mean\ ash\ in\ raw\ BCBA} \times 100 \tag{6}$$

The detailed main effects and interaction plots supporting these results are provided in Supplementary Information A (Fig. S1 and S2). Main effects analysis shows that the solid-to-liquid ratio had the strongest influence on ash removal, with greater dilution (1/15) producing the lowest mean ash mass due to improved cavitation and reduced particle shielding. Ultrasonic amplitude had a secondary effect; increasing amplitude generally increased measured ash mass, suggesting that excessive cavitation energy may promote re-deposition or fragmentation rather than net removal. Sonication time showed a non-linear trend: 1 min was insufficient, 5 min gave no consistent improvement, and 3 min provided the lowest and most stable ash values, indicating an optimal exposure time. Interaction plots reveal notable interactions between ratio and amplitude, and between amplitude and time. At high

Table 1
Ash determination for all ash removal methods.

Method	Sample/ Particle size (mm)	Sample mass (g)	Mean ash mass (with standard deviation (g)	Ash content (%)	Ash removal efficiency (%)
No pre-processing	Raw BCBA	2.00	0.108 ± 0.002	5.40	–
Ball milled & sieved	≥ 1.4	2.00	0.038 ± 0.004	1.91	64.69
Ball milled, sieved & rinsed with sonication probe	≥ 1.4	2.00	0.027 ± 0.001	1.33	75.44

dilution (1/15), the effect of amplitude diminished, whereas at low dilution (1/5), higher amplitude and longer time tended to increase ash mass, highlighting the need to control energy input under concentrated conditions. Overall, the most effective and reproducible conditions were a 1/15 ratio, 25% amplitude, and 3 min sonication, yielding consistently low ash contents (~1.6–1.8 wt%) with minimal variability.

3.2. Precursor characterisation

Proximate and ultimate analyses were conducted to observe the thermal behaviour and elemental composition of both precursors, i.e. uB_S and ESP, providing insight into their suitability for carbonisation and catalytic modification (Table 2). Proximate analysis of uB_s revealed a significant proportion of volatile organic matter (VOM) relative to FC and residual ash. The reduction in ash content compared to raw BCBA confirms the efficacy of the size separation and ultrasonic washing step. This reduction is critical for improving carbon yield and minimising pore blockage during subsequent pyrolysis and activation. On the other hand, the reduction in FC compared to raw BCBA can be attributed to size reduction experiments where some fixed carbon has been lost in lower fractions left unused [41]. Moisture content was low, consistent with the moisture content of oven-dried wood [42]. These results indicate that the prepared uB_S provides a baseline suitable for controlled pyrolysis and subsequent surface modification. In contrast, ESP exhibited negligible moisture and FC contents, with 'volatile matter' of about 45%. This VOM quantity mainly reflects thermal decomposition of $CaCO_3$, not organic volatiles. This explains why the proximate analysis of ESP shows high VOM despite being predominantly inorganic.

Ultimate analysis further demonstrated that uB_s was dominated by carbon (~50%), with appreciable hydrogen content and negligible nitrogen and sulphur - supporting its role as a viable carbon precursor. Similarly, ultimate analysis of ESP indicated minimal carbon content associated primarily with carbonate species, while hydrogen, nitrogen, and sulphur were below detectable limits. These findings reinforce the role of ESP as a calcium-rich mineral additive rather than a carbon source.

SEM analysis revealed distinct morphological differences between the two main precursors (Fig. 3b and c). BCBA particles displayed irregular, fibrous, and fractured surfaces, characteristic of partially combusted lignocellulosic material (Fig. 3a). The preserved cellular architecture, including elongated fibres and voids corresponding to vascular channels, indicates that a significant fraction of the original biomass structure remained intact despite exposure to high-temperature combustion conditions within Drax boilers. uB_s, on the other hand, exhibited visibly cleaner surfaces, with a marked reduction in adherent fine particulates compared to the raw material. The removal of loosely bound mineral ash exposed the underlying biomass texture and enhanced surface accessibility. The reduced surface encrustation and improved definition of cell wall features, supporting the effectiveness of ultrasonication in selectively removing inorganic residues without excessive damage to the biomass framework. ESP particles, by contrast, exhibited angular morphologies with relatively smooth surfaces and sharp edges.

EDS analysis corroborated these observations (Table 3). BCBA contained detectable levels of inorganic elements such as calcium, potassium, silicon, magnesium and aluminium, consistent with ash deposition during combustion. After ultrasonic treatment, the relative intensity of these elements decreased substantially, while carbon and oxygen became dominant in the spectra, confirming successful demineralisation of the biomass surface. On the other hand, EDS spectra of ESP were dominated by calcium and oxygen, with minor contributions from carbon and trace amounts of magnesium and sulphur, reflecting the calcium carbonate-rich composition of eggshells.

Collectively, SEM-EDS analysis highlights the complementary nature of the two waste precursors: the biomass provides a structurally intact, carbon-rich framework suitable for pore development, while eggshells serve as a concentrated inorganic calcium source capable of influencing catalytic reactions during pyrolysis and activation.

The XRD pattern of uB_S exhibits the characteristic features of lignocellulosic materials dominated by cellulose I (Fig. 4). The intensity in the pattern is represented as counts; however, it is important to note that the intensity unit is arbitrary and has no physical meaning. The uB_s XRD pattern reveals a broad diffraction peak centred at approximately $2\theta = 22.5^\circ$ which corresponds to the (002) crystalline plane of native cellulose, while a less intense shoulder observed around 15–16° is associated with the overlapping (101) reflection and contributions from amorphous cellulose, hemicellulose, and lignin. The elevated background intensity at low diffraction angles and the absence of sharp Bragg reflections indicate a predominantly amorphous structure with limited long-range order. The crystallinity index (*CrI*) was estimated using the Segal method [43], where I_{002} is the maximum intensity of the cellulose *I* crystalline peat at $2\theta \backsimeq 22–23^\circ$ and I_{am} is the intensity of the amorphous region at $2\theta \backsimeq 18^\circ$ (Eq. (7)). This provides a semi-quantitative assessment of the relative crystalline cellulose content. The calculated *CrI* was approximately 42%, confirming the semi-crystalline nature of the raw biomass. This relatively low crystallinity is typical of untreated lignocellulosic feedstocks and is advantageous for subsequent thermal conversion. Crystallite size estimation was not undertaken because the broad diffraction features and substantial amorphous contribution render Scherrer analysis unreliable for this material.

$$CrI\ (\%) = \frac{I_{002} - I_{am}}{I_{002}} \times 100 \tag{7}$$

In contrast, ESP exhibited well-defined diffraction peaks corresponding to crystalline calcite ($CaCO_3$) (Fig. 4), confirming the high crystallinity and phase purity of the eggshell precursor. The most intense peak is observed at $2\theta \approx 29.44^\circ$, corresponding to the (104) crystallographic plane of calcite. Additional prominent reflections appear at $2\theta \approx 23.11^\circ$, 35.98°, 39.49°, 43.18°, 47.54°, 48.59°, 57.45°, 60.66°, 65.98°, and 73.14°, which can be indexed to the (012), (110), (113), (202), (018), (116), (122), (214), (300), and (119) planes of calcite, respectively. These diffraction peaks are in excellent agreement with the standard reference pattern for calcite - the International Centre for Diffraction Data (ICDD PDF No. 00–066-0867), confirming that the predominant crystalline phase in the eggshell is calcium carbonate in its calcite polymorph. The absence of additional significant peaks indicates high phase purity, with no detectable secondary crystalline phases within the instrument detection limits. Hence, further semi-quantitative phase analysis was not considered necessary. Also, no amorphous features were observed, indicating that ESP serves primarily as a crystalline inorganic source of calcium rather than a structural carbon component.

Physisorption analysis of the uB_s sample at 77 K using N_2 adsorbate exhibited an isotherm trend typical of Type IVa isotherms (as shown in Supplementary Information B). This indicates limited N_2-accesible

Table 2
Composition of precursors obtained from proximate and ultimate analysis.

Sample	Ultimate Analysis (wt%)				Proximate Analysis (wt%)			
	Carbon	Hydrogen	Nitrogen	Sulphur	Moisture	VOM	Fixed Carbon	Ash
BCBA	48.25	6.09	0.20	0.10	5.06	67.23	25.47	2.24
uB_S	50.02	5.78	0.17	0.00	6.08	74.96	17.02	1.94
ESP	12.54	0.33	0.48	0.00	0.38	45.69	0.00	53.93

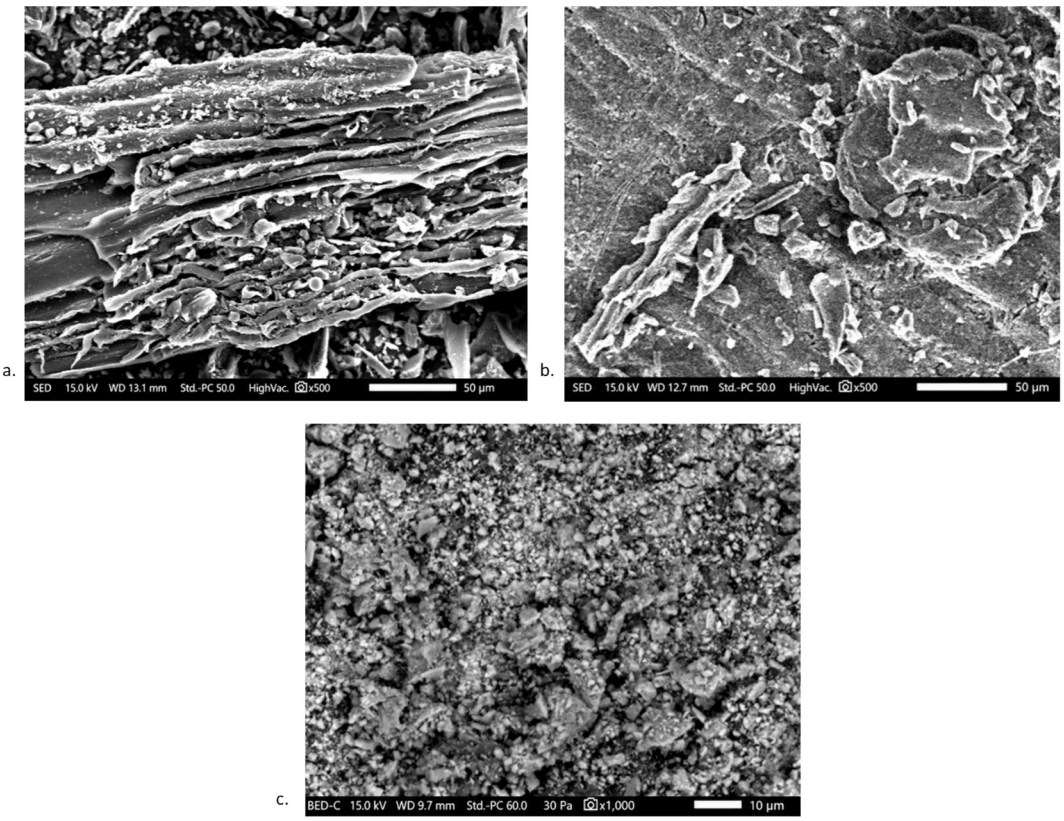

Fig. 3. SEM images of a) BCBA, b) uB_S and c) ESP.

Table 3
Surface elemental composition of precursors via EDS.

Element	Composition (wt%)		
	BCBA	uB_S	ESP
C	55.8	55.2	11.8
O	41.3	44.1	42.0
Ca	1.8	0.6	44.2
Si	0.6	0.1	0
Mg	0.2	0	0.2
Al	0.2	0	0
K	0.1	0	0
S	0	0	0.1

mesoporosity, while the sharp uptake at high relative pressure suggests the presence of larger pores or interparticle voids. This suggests the uB_S sample porosity is dominated by macroporous cellular features that are not fully characterised by N_2 adsorption. The BET fitting range was selected between relative pressure values 0.1 to 0.35 based on the linear region of the BET transform with C constant identified as 10.80 and using the Rouquerol criteria [44]. This range provided a physically meaningful fit for sonicated wood and gave a BET total surface area value of 37.38 m^2g^{-1} (Table 5). The t-plot analysis further gave an external surface area of 29.98 m^2g^{-1}, with the linear region found at relative pressure between 0.25 and 0.5. Both theories use different relative pressure ranges for linearisation as they have different adsorption assumptions. Since the external surface area was identified to be lower than the BET total surface area, this proved the result was physically consistent with the BET method for measuring total accessible area (which includes external surface area and microporous contributions). The total pore volume of all samples were calculated from the N_2 adsorption isotherms using Eq. (8); where V is total pore volume, V_{ads} is adsorbed nitrogen volume at $P/P_0 \simeq 1$, M is molecular weight of N2, ρ is density of liquid N2 at 77 K and 22,414 is the molar volume of ideal gas at standard temperature and volume in cm3mol-1. After calculation, the total pore volume for the uB_S was 0.046 $cm^3\ g^{-1}$ with an average pore size of 39.05 nm. Overall, both BET- and t-plots show that the wood possesses a moderately porous structure with predominantly external surface adsorption characteristics. For this sample, CO_2 adsorption analysis was not considered necessary due to the incredibly low microporous contribution indicated by the N_2 adsorption results. Additionally, natural wood materials are generally characterised by cellular macroporous and mesoporous structures arising from vessels, lumina and fibres, rather than developed microporous frameworks typical of synthesised carbons. Physisorption analysis was mainly conducted in uB_S to give a base comparison with the synthesised chars, and all data has been included in Supplementary Information B.

$$V = \frac{V_{ads} \times M}{22414 \times \rho} \tag{8}$$

3.3. Dual-response optimisation of pyrolysed (eggshell-free) biomass

The pyrolysis behaviour of uB_S was optimised using a dual-response face-centred central composite design, with FC content and char yield selected as performance metrics (full design in provided in Table S4 in supplementary information A). These responses reflect competing objectives: maximising carbon enrichment while retaining sufficient solid yield for practical adsorbent production. The influence of pyrolysis temperature, heating rate, and residence time was evaluated through main-effects, interaction, and three-dimensional response surface plots.

3.3.1. Main effects & interaction plots

Main-effects analysis revealed pyrolysis temperature as the dominant factor governing both FC content and char yield (Fig. 5). Increasing the temperature resulted in a pronounced increase in FC content, rising from approximately 64% to over 84%, driven by enhanced devolatilisation and progressive aromatisation of the biomass matrix. Conversely,

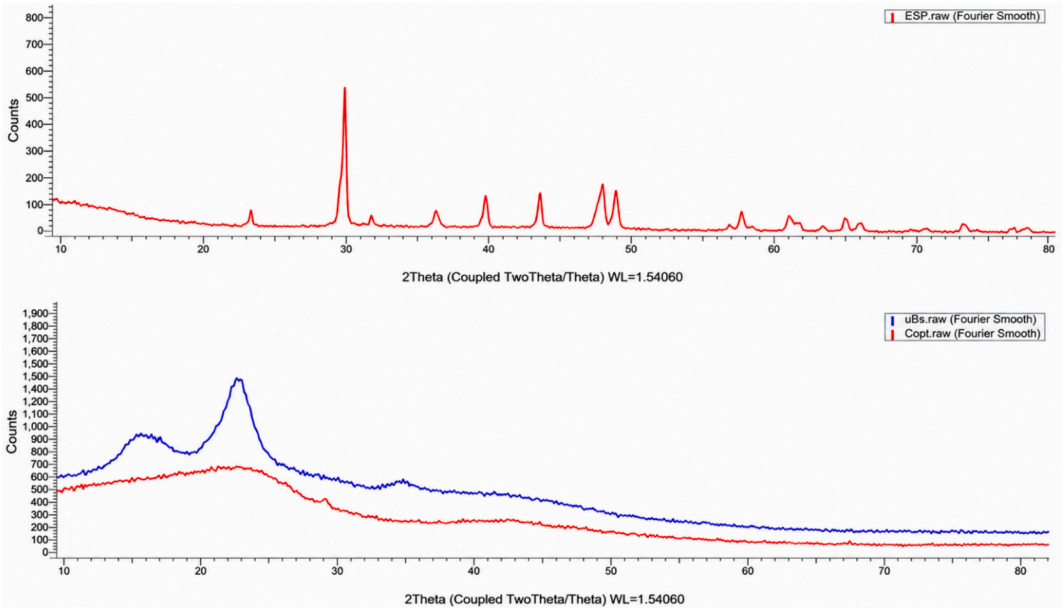

Fig. 4. XRD patterns of ESP, uB_S and C_{opt}.

char yield declined sharply with increasing temperature, decreasing from ~42% to ~30%, reflecting intensified thermal decomposition and mass loss at elevated temperatures. Heating rate exerted a secondary influence on both responses. Moderate heating rates (~15 °C min^{-1}) favoured higher FC content, likely due to improved control over volatile release and secondary char-forming reactions. Very high heating rates reduced FC slightly and increased variability, suggesting incomplete structural rearrangement during rapid thermal exposure. Char yield exhibited a shallow minimum at intermediate heating rates, indicating a balance between devolatilisation kinetics and solid-phase stabilisation. Residence time showed a non-monotonic effect. Intermediate hold times (~60 min) maximised FC content, while extended residence (90 min) provided no further improvement and marginally reduced FC content. Short hold times (30 min) were insufficient to complete carbonisation, resulting in lower FC values. These trends suggest diminishing returns beyond an optimal residence time.

Interaction plots (Fig. S3 in supplementary information A) highlight significant temperature-time and temperature-heating rate interactions. At higher temperatures, prolonged hold times exacerbated yield losses without proportionate FC gains. Similarly, increasing heating rate at elevated temperatures reduced both yield and FC stability. In contrast, interactions were minimal at lower temperatures, indicating greater process robustness under mild pyrolysis conditions.

3.3.2. *Contour & 3-D surface plots*

Contour plots and three-dimensional response surface plots (Fig. S4 – S7 in supplementary information A) further illustrate the trade-off between FC content and char yield across the design space. Regions of high FC (>80%) are confined to high-temperature regimes (>700 °C) combined with moderate heating rates and intermediate hold times. However, these conditions coincide with low char yields (<32%), limiting practical material throughput.

Conversely, high char yields (> 40%) are observed at low temperatures (< 450 °C), but at the expense of insufficient carbon enrichment. The optimal compromise region is located at intermediate temperatures (~600–650 °C), moderate heating rates (~10–15 °C min^{-1}), and residence times of 50–70 min, where FC content exceeds 75% while char yield remains above 34%. This region represents a balanced operating window suitable for scalable adsorbent production.

3.3.3. *Multiple-response prediction & validation*

Multiple-response optimisation was performed to identify pyrolysis conditions that balance carbon enrichment with material yield. Individual optimisation of FC content and char yield revealed distinctly different operating regimes as predicted by the Minitab software (Table 4). Maximisation of FC content alone favoured severe pyrolysis conditions, yielding a high predicted FC content of 86.5%. However, these conditions are associated with substantial mass loss and were therefore unsuitable for practical sorbent production. Conversely, maximisation of char yield alone was achieved under mild pyrolysis conditions, producing a high yield of 44.1% but insufficient carbon enrichment for adsorption applications. These results highlight the intrinsic trade-off between yield retention and carbonisation severity. Simultaneous optimisation of both responses identified an intermediate operating window as the most desirable compromise. The combined-response model predicted optimal conditions at 521.2 °C, a heating rate of 5 °C min^{-1}, and a hold time of 90 min, resulting in a char yield of 36.7% and an FC content of 77.4%. This condition maximises overall desirability by preserving a substantial fraction of solid yield while achieving a sufficiently high level of carbon enrichment.

Experimental validation performed at the predicted combined optimum produced results in close agreement with model predictions (Table S5 in supplementary information A), confirming the robustness of the optimisation strategy.

3.4. *Characterisation & analysis of optimum pyrolyzed (eggshell-free) char*

C_{val}, obtained via the dual-response optimisation identified in Section 3.3, was comprehensively characterised to establish its physicochemical properties prior to eggshell-based surface modification and activation. This baseline characterisation provides a reference framework for assessing the structural, chemical, and textural evolution induced by calcium incorporation and physical activation in subsequent sections. Proximate analysis of C_{val} confirms successful carbonisation of the biomass precursor. The material exhibits a high FC content (Table S4 in supplementary information A), consistent with the dual-response optimisation target, leaving substantially reduced volatile matter relative to the untreated biomass. This compositional profile indicates a stable carbon matrix with minimal inorganic interference, which is advantageous for controlled activation and surface functionalisation.

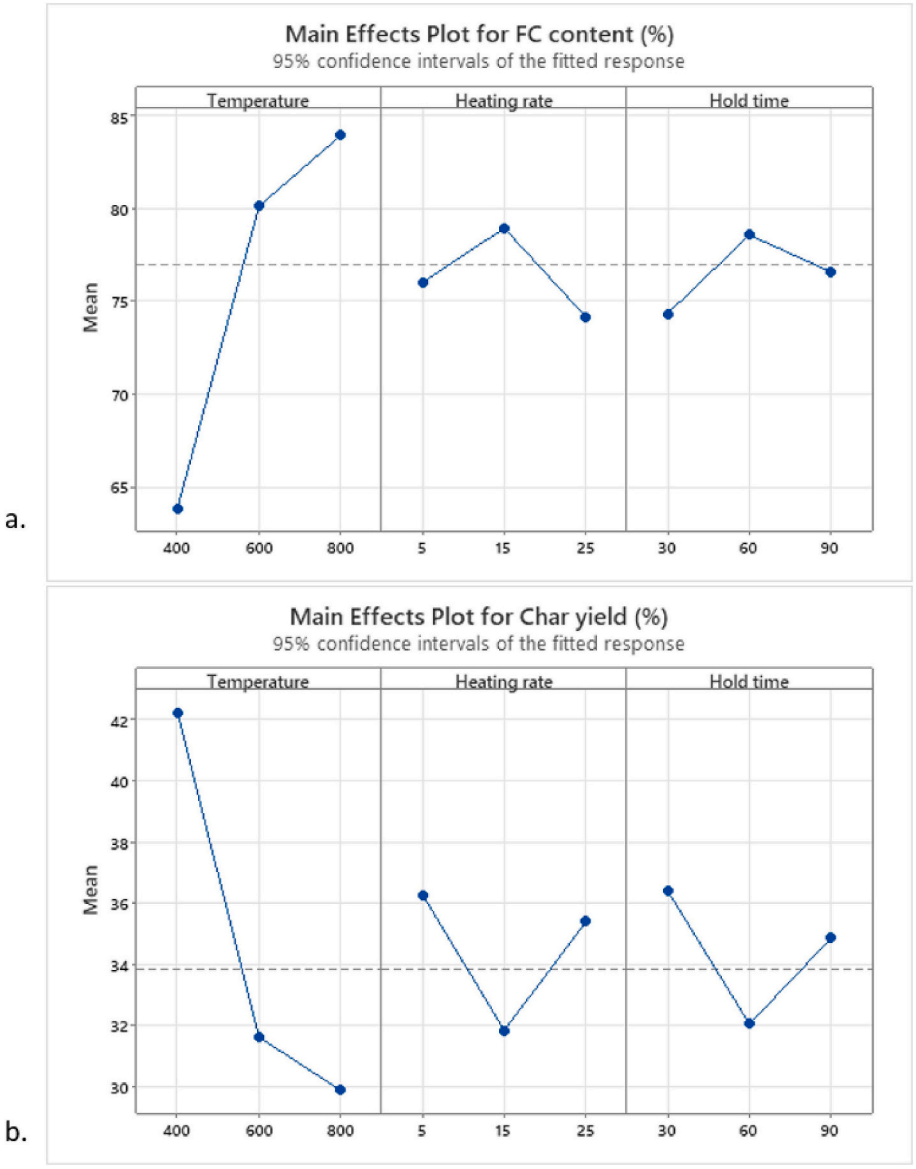

Fig. 5. Main effects plots for eggshell-free pyrolysis – a) FC content and b) char yield. 95% confidence intervals of the fitted mean response were obtained from the response surface model.

Table 4
Optimum response prediction for eggshell-free pyrolysis.

Response	Goal	Temperature (°C)	Heating rate (°C min^{-1})	Hold time (min)	Char yield (%)	FC Content (%)
FC content	Maximise	755.6	10.86	90.00	–	86.50
Char yield	Maximise	400.0	25.00	30.00	44.11	–
FC content + Char yield	Maximise	521.2	5.00	90.00	36.65	77.40

Table 5
Surface area and pore size distribution summary for all physisorption analysis.

Sample	Surface Area (m^2 g^{-1})			Pore Volume (cm^3 g^{-1})		Average Pore Size (nm)	
	BET (N_2 77 K)	t-plot (external) (N_2 77 K)	NLDFT (micropore) (CO_2 273 K, P/P_0: 0–0.035)	Total (N_2 77 K, P/P_0: 0–1)	NLDFT (micropore) (CO_2 273 K, P/P_0: 0–0.035)	NLDFT (N_2 77 K, P/P_0: 0–1)	NLDFT (CO_2 273 K, P/P_0: 0–0.035)
uB_s	37.38	29.96	–	0.046	–	39.05	–
C_{val}	153.62	103.29	66.99	0.081	0.023	2.79	0.93
C_{opt}	4.47	3.57	335.99	0.007	0.094	2.37	1.00
AC_{opt}	463.38	92.03	384.29	0.299	0.091	2.85	0.88

A combination of N_2 and CO_2 physisorption analysis was conducted on C_{val} using the procedure outlined in Section 2.5 (all data shown in supplementary information B). The BET total accessible surface area obtained from N₂ adsorption at 77 K (153.62 $m^2\ g^{-1}$) was higher than the external surface area determined from the t-plot method (103.29 $m^2\ g^{-1}$) (Table 5). The BET range that satisfied Rouquerol criteria [44] was at relative pressures 0.05 to 0.3 with C constant 9.16; however, since N_2 adsorption does not accurately quantify microporous structure of the material, complementary CO_2 adsorption was conducted at 273 K to measure the microporous surface area. t-plot on the other hand, used a different relative pressure range (0.29 to 0.75) as the two methods rely on different adsorption assumptions and linearisation criteria. The t-plot analysis exhibited moderate linearity ($R^2 = 0.7763$), indicating low conformity with the assumptions of the model. This behaviour suggests limited microporous development. To confirm, CO_2 adsorption at 273 K was conducted revealing a micropore surface area of 66.99 $m^2\ g^{-1}$, as identified using NLDFT - indicating the presence of more micropores inaccessible to N_2 at cryogenic temperature. The slight discrepancy arises from diffusion limitations and restricted pore accessibility of N_2 in narrow micropores, whereas CO_2 at 273 K exhibits enhanced diffusivity and more effective probing of ultra microporosity. The total pore volume of C_{val} was calculated using Eq. (8) and found to be 0.081 $cm^3\ g^{-1}$. The pore size distribution and average mesopore size (2.79 nm) were derived using the NLDFT method based on the N_2 isotherm. In contrast, the micropore volume (0.023 $cm^3\ g^{-1}$) and average micropore size (0.93 nm) were calculated from CO_2 isotherms using the NLDFT. These results confirm that the material is predominantly ultra microporous, with microporosity underestimated by N₂ adsorption analysis. Hence, only CO_2 isotherms (with NLDFT pore size distribution) have been included in this paper (Fig. 6 and Fig. 11). It is important to note that the pore volume recorded in Table 5 was obtained from the N_2 or CO_2 adsorption isotherm at the highest measurable relative pressure. The N_2 isotherm indicates the coexistence of micropores and mesopores, evidenced by the initial steep uptake and the presence of a small hysteresis loop typical of Type IV isotherms (and has been included in supplementary information B). In contrast, the CO_2 isotherm exhibits a typical Type I profile with rapid adsorption at low relative pressures, confirming the presence of ultra micropores. This behaviour is typical of chars produced under moderate pyrolysis conditions and confirms that pore generation is not yet fully developed at this stage. While unsuitable as a high-capacity adsorbent, the low baseline surface area provides a clear platform for quantifying porosity enhancement following eggshell-assisted modification and physical activation.

SEM analysis of C_{val} revealed partial preservation of the fibrous biomass architecture, with collapsed cell walls and the emergence of surface fissures resulting from devolatilisation during pyrolysis. The surface morphology remains relatively dense, with visible pore openings, consistent with the physisorption results. At the magnification shown (x500), the char surface appears heterogeneous and densely packed, with elongated grooves and irregular cavities aligned along the biomass fibre direction (Fig. 7). These features indicate anisotropic shrinkage of the carbon matrix during thermal treatment. While some pore openings and voids are visible, they appear to be predominantly macroporous and poorly interconnected, confirming that extensive pore development has not yet occurred at this stage. This observation is consistent with the low surface area measured prior to activation and reflects the non-activated nature of the char.

The EDS spectra of C_{val} identified carbon and oxygen as the dominant elements, with only trace levels of residual inorganic species such as calcium (Table 6). This elemental composition is beneficial for subsequent impregnation with eggshell-derived calcium species, as it reduces competitive mineral interactions. Overall, the SEM–EDS analysis demonstrates that the optimised eggshell-free char possesses a structurally intact but weakly porous carbon framework. This morphology provides a favourable baseline for controlled pore generation and surface modification in later processing stages.

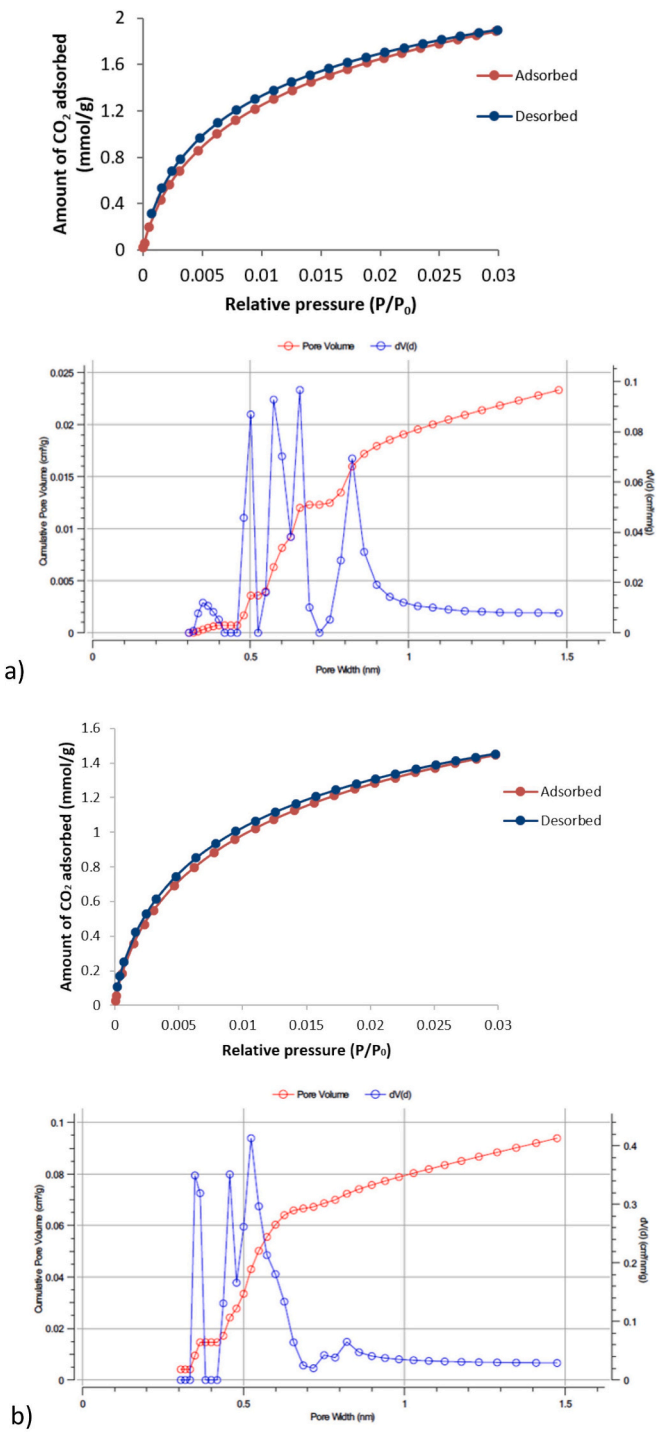

Fig. 6. a) CO_2 adsorption-desorption isotherm (top) and pore size distribution (bottom) for C_{val} b) CO_2 adsorption-desorption isotherm (top) and pore size distribution (bottom) for C_{opt} using NLDFT model obtained from physisorption analysis with CO_2 adsorbate.

3.5. Identification of optimum surface-enhanced char

3.5.1. Dry-mixing experiments

Dry-mixing experiments were conducted to assess the impact of physically blending calcined eggshell powder with biomass char at increasing eggshell loadings: 5–25 wt% on a uB_s basis (Table S6 in supplementary information A). The results demonstrate an obvious diminish in fixed carbon and CO_2 uptake with an increase in ESP, as summarised by the interval plots (Fig. S8). This reduction reflects a

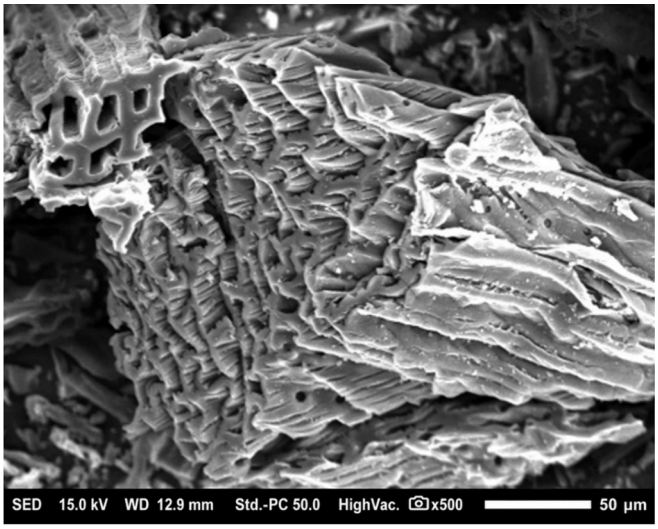

Fig. 7. SEM image of eggshell-free pyrolysed char at x500.

Table 6
Surface elemental composition of eggshell-free and modified chars via EDS.

Element	Average Composition (wt%)		
	C_{val}	C_{opt}	AC_{opt}
C	89.5	66.7	67.4
O	9.1	25.0	21.7
Ca	1.4	8.3	9.5

dilution effect, where increasing inorganic content progressively replaces carbonaceous material rather than enhancing carbon structure or porosity. As dry mixing does not promote chemical interaction or catalytic activity between calcium species and the carbon matrix, no compensatory increase in carbon retention or structural development is observed. Char yield was also monitored (though not utilised as a response in the OFAT design) and from observation increased progressively with increasing eggshell amounts, indicating that the addition of thermally stable, mineral-rich eggshell material contributes directly to higher residual solid yield. This behaviour is consistent with the high $CaCO_3$/CaO content of eggshells, which does not volatilise during thermal treatment and therefore, inflates the apparent char yield.

These results indicate that while dry mixing is effective for increasing overall char yield and surface alkalinity, excessive eggshell loading leads to significant loss of fixed carbon fraction. Consequently, low eggshell ratios ($\leq$ 10 wt%) represent a practical upper limit for dry-mixed samples where carbon integrity remains acceptable. However, the inability of this method to enhance internal surface area or microporosity limits its suitability for high-performance adsorption applications.

3.5.2. Impregnation experiments

Calcium-ion impregnation experiments were carried out to enable controlled incorporation of calcium species within the carbon matrix and to promote catalytic effects during thermal treatment. The effects of CaA/uB_S ratio (0.25–0.75 wt%) and dosing time (30–150 min) on FC content and CO_2 uptake were systematically evaluated. The experimental data has been included in Table S7 of supplementary information A. At low calcium loadings (0.25 wt%), the impregnated samples exhibited the highest CO_2 uptake (~0.6 mmol g^{-1}) alongside a high FC content (61.1–70.72%). This indicates effective dispersion of Ca^{2+} ions (at (0.25 wt% loading) within the carbon structure, which upon pyrolysis form highly distributed CaO catalytic sites, preventing over-gasification and minimising pore collapse. These sites promote controlled gasification via key reactions such as the Boudouard reaction (Eq. (2)), the water-gas reaction (Eq. (9)), and the reversible carbonation of CaO (Eq. (10)) [45]. Increasing the dosing time at the same calcium loadings did not contribute any substantial change in either FC content or CO_2 uptake. This means that longer dosing times did not facilitate more surface interactions between calcium ions and the carbon matrix. On the other hand, increasing calcium loadings caused a decrease in both responses.

$$C + H_2O \rightarrow CO + H_2 \quad (9)$$

$$CaO + CO_2 \rightleftharpoons CaCO_3 \quad (10)$$

The factorial design was modelled for response optimisation using regression model. The model seemed to fit the data well for both FC content and CO_2 uptake (R^2 = 95.44% and R^2 = 95.97%, respectively) and gave moderate predictive ability (~50%) for both. The design was then optimised to maximise both responses. The optimum impregnation conditions were found to be low calcium loading (0.25 wt%) at high dosing time (150 min) as predicted in Minitab (Table 7). This was experimentally validated and had similar results as the predicted values. Overall, Ca-ion impregnation proved significantly more effective than dry mixing for surface enhancement, provided calcium loading and dosing time were carefully controlled. These findings highlight the critical importance of calcium dispersion and chemical interaction in designing surface-enhanced chars for adsorption applications.

3.6. Characterisation & analysis of optimum surface-enhanced char

The optimum surface-enhanced char (C_{opt}), identified through Ca-ion impregnation under low calcium loading and high dosing time, was subjected to comprehensive physicochemical characterisation. This was done primarily to confirm improvements in carbon structure, surface chemistry, and textural properties relative to both the raw biomass and the eggshell-free pyrolysed char. All analyses integrated understanding of the role of calcium in enhancing surface functionality while preserving carbon integrity.

Proximate analysis of the C_{opt} revealed a high FC content with a controlled ash fraction, indicating effective incorporation of calcium without excessive mineral dilution (Table 8). In comparison with FC content of C_{val} (Table S4 in supplementary information A), the Ca-enhanced sample retained a substantial proportion of FC, confirming that the selected impregnation conditions avoided over-catalytic gasification during thermal treatment. The increase in ash content is attributed to the presence of calcium species introduced during impregnation and is consistent with successful surface modification rather than bulk mineral accumulation. VOM significantly reduced, indicating a well-developed carbon framework and effective devolatilisation. Overall, the proximate analysis confirms that the optimum surface-enhanced char achieves a favourable balance between carbon retention and inorganic functionalisation. Similarly, ultimate analysis of the surface modified char (Table 8) indicated an increase in the composition of carbon compared to uB_s (Table 2) which is like attributed to carbonisation which occurs during pyrolysis of impregnated biomass. AC_{opt} can be seen with a slight reduction in carbon due to the formation of new pores during CO_2 activation.

The porosity analysis of C_{opt} (all data in Supplementary Information

Table 7
Optimum response prediction (from Minitab) for impregnation experiments.

Response	Goal	CaA/uB_s (wt% uB_s basis)	Dosing time (min)	FC Content (%)	CO_2 uptake (mmol g^{-1})
FC content	Maximise	0.25	30.00	68.35	–
CO_2 uptake	Maximise	0.28	119.70	–	0.64
FC content + CO_2 uptake	Maximise	0.25	150	67.89	0.64

Table 8
Composition of C_{opt} and AC_{opt}.

Sample	Ultimate Analysis (wt%)				Proximate Analysis (wt%)			
	Carbon	Hydrogen	Nitrogen	Sulphur	Moisture	VOM	Fixed Carbon	Ash
C_{opt}	65.96	2.47	0.20	0.00	2.67	17.31	69.21	10.81
AC_{opt}	65.11	0.73	0.41	0.00	2.01	13.53	61.08	23.42

B) suggested that BET model was not highly applicable to the N_2 adsorption isotherm at 77 K, as it produced low BET and external surface areas, typically because of dominant micropore filling at low relative pressures, which is beyond the scope the BET model theory. The BET range that satisfied the Rouquerol criteria [44] was in the very low relative pressure region (0.02 to 0.07) with C constant 80.38, giving a BET total surface area of 4.47 $m^2\ g^{-1}$. The t-plot linear region was found to be the entire relative pressure region (0–1) giving an R^2 value of 0.9957 and yet gave a low external surface area. The external surface area estimated from the t-plot method was found to be 3.57 m^2g^{-1} indicating that adsorption was likely dominated by micropore filling and that the calcium species was acting as a pore-blocking or templating agent (which could subsequently enable the formation of a more open pore structure during activation). This was confirmed by measuring the microporous surface area (335.99 m^2g^{-1}) by CO_2 adsorption at 273 K using NLDFT (Table 5). The total pore volume of C_{opt} was determined from the N_2 adsorption isotherms at a relative pressure ($P/P_0 \backsimeq 1$) and was found to be 0.007 $cm^3\ g^{-1}$. Since the N_2 adsorption isotherm suggested BET model was not highly applicable, the low total pore volume cannot be relied on for this sample. However, the pore size distribution and average mesopore size (2.37 nm) were derived using the NLDFT method based on the N_2 isotherm. In contrast, the micropore volume (0.094 $cm^3\ g^{-1}$) and average micropore size (1 nm) were calculated from CO_2 isotherms using the NLDFT in the pore size range 0.2–1.5 nm. The pore size distribution can be seen in Fig. 6b.

The CO_2 isotherm exhibited characteristics consistent with a predominantly microporous material, with minimal hysteresis (Fig. 6b), indicating developed and accessible pore networks rather than mesopore-dominated structures. The CO_2 isotherm was a typical Type I isotherm unlike the N_2 isotherm which exhibited a Type IVa behaviour with an H3 hysteresis loop indicating capillary condensation within mesopores, The substantial increase in microporous surface area after the introduction of calcium species is consistent with literature [33,35] suggesting that well-dispersed Ca^{2+} ions (transformed into CaO during thermal treatment) promoted micropore development through catalytic carbon conversion via the Boudouard and water-gas reactions (Eq. (2) and Eq. (9)), leading to controlled burn-off of the carbon matrix as well as lowering the activation energy required for gasification and enabling effective pore development. The physisorption results therefore, validate the modification strategy adopted in this study.

SEM analysis of C_{opt} char revealed a well-preserved carbon morphology with clear evidence of surface textural modification following Ca-ion impregnation. The carbon matrix exhibited roughened surfaces and the presence of newly developed pore openings (*Fig. 8*a), consistent with the enhanced surface area observed in physisorption analysis. The best impregnated sample (C_{opt}) was compared with the best dry mixed sample ($C_{DM\text{-}5wt\%}$) at lower magnifications to observe any calcium residues (*Fig. 8*b and c). The dry mixed sample showed calcium-rich phases which appeared brighter in spectra because of its relatively higher atomic number than surrounding lighter elements. Unlike $C_{DM\text{-}5wt\%}$, no large agglomerates of calcium-rich phases were observed in C_{opt}, indicating effective dispersion of calcium species

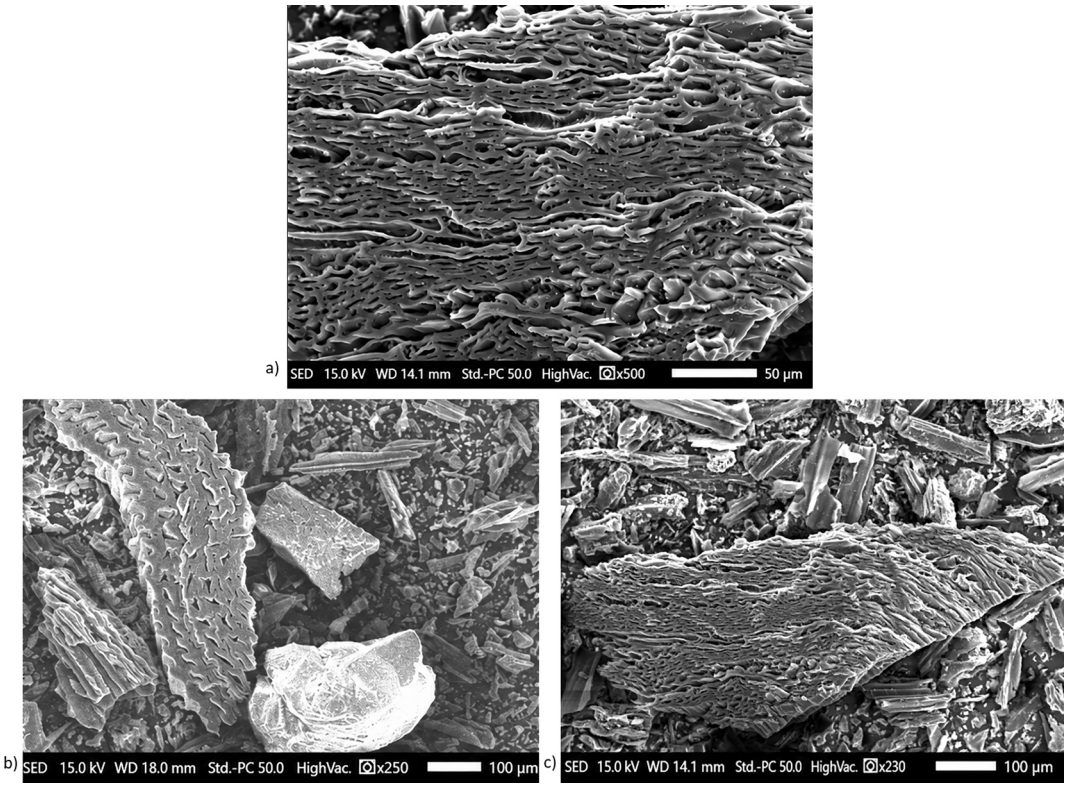

Fig. 8. SEM image of a) C_{opt} at x500, b) $C_{DM\text{-}5wt\%}$ at x250 and c) C_{opt} at x230.

throughout the carbon framework. EDS results for C_{opt} shows a substantial reduction in carbon content (66.7 wt%) (Table 6) accompanied by a marked increase in oxygen (25.0 wt%) and calcium (8.3 wt%). This shift confirms successful incorporation of calcium species onto or within the char surface, most likely as Ca-containing phases such as CaO, $Ca(OH)_2$, or $CaCO_3$ formed during pyrolysis. The increased oxygen content further suggests that impregnation promotes the retention or formation of oxygen-containing surface functionalities and inorganic oxygenated phases. The combined SEM-EDS results confirm that Ca-ion impregnation promotes surface-level modification rather than bulk mineral loading, preserving the structural integrity of the char.

Based on the XRD pattern (Fig. 4), C_{opt} shows the disappearance of the characteristic cellulose I reflections observed in uB_s [43], confirming the thermal decomposition of the crystalline lignocellulosic structure and the formation of a carbonaceous matrix. A broad diffraction peak centred at approximately $2\theta = 22–25^\circ$ is assigned to the (002) reflection of turbostratic carbon, indicating a predominantly amorphous structure with limited graphitic ordering. A weak, broad feature around $2\theta \approx 43^\circ$ corresponds to the overlapping (100)/(101) reflections of disordered aromatic carbon domains. No distinct crystalline calcium-containing phases were detected within the XRD detection limits, suggesting that eggshell-derived calcium is either highly dispersed, present in low concentrations, or exists in an amorphous form. Although XRD alone cannot confirm the catalytic role of calcium, the observed structural evolution is consistent with literature describing calcium-assisted carbonisation of biomass-derived carbons [33]. Overall, the diffraction pattern indicates that pyrolysis produced a poorly ordered carbon framework, which is favourable for subsequent pore development during activation.

Raman spectroscopy was employed to evaluate structural ordering and defect density within the optimum surface-enhanced char compared to unprocessed biomass and unmodified char (Fig. 9). All three samples exhibit the characteristic D (~1350 cm^{-1}) and G (~1580–1600 cm^{-1}) bands associated with disordered and graphitic sp^2 carbon structures, respectively. In uB_s, the broad and relatively low-intensity D and G bands reflect the presence of small, poorly organised aromatic clusters originating primarily from lignin, with an I_D/I_G ratio of 0.656 confirming a predominantly amorphous structure lacking extended graphitic ordering. Upon impregnation and carbonisation (C_{opt}), both bands become more defined, indicating progressive aromatisation and structural reorganisation. The slight reduction in I_D/I_G to 0.644 suggests marginal growth of sp^2 domains and improved ordering of turbostratic carbon layers, although the change remains modest, implying limited graphitisation. For C_{val}, the D and G bands are similarly well developed, with an I_D/I_G value of 0.652. This value, comparable to that of uB_s and C_{opt}, indicates that while thermal treatment enhances aromatic condensation and structural maturity, the material retains a significant degree of disorder. The proximity of all I_D/I_G ratios (0.644–0.656) suggests that processing primarily promotes reorganisation and condensation of existing aromatic clusters rather than a substantial transition toward highly ordered graphite-like structures. Furthermore, the weak and broad second-order (2D) features across all samples between 2600 and 2750 cm^{-1}, confirming that the carbons remain predominantly turbostratic with limited graphitic stacking. Overall, the Raman analysis demonstrates progressive structural evolution from lignocellulosic precursor to carbonised materials, with moderate enhancement in aromatic ordering while preserving defect-rich domains that are beneficial for adsorption-driven applications such as CO_2 capture and wastewater treatment.

The FTIR spectra of uB_s, C_{val}, and C_{opt} (4000–500 cm^{-1}) reveal progressive transformation from lignocellulosic biomass to carbonised char (Fig. 10). In uB_s, the sharp feature at ~3700–3600 cm^{-1} and the broad band at ~3500–3200 cm^{-1} correspond to O—H stretching vibrations from free and hydrogen-bonded hydroxyl groups in cellulose, hemicellulose and lignin. The absorption around ~2920–2850 cm^{-1} is assigned to aliphatic C—H stretching of $-CH_2$ and $-CH_3$ groups, indicating intact polysaccharide structures. The strong peak near ~2350 cm^{-1} is attributed to atmospheric CO_2 in the optical path, which is commonly observed in FTIR measurements. The band around ~1600–1580 cm^{-1} is associated with aromatic C═C skeletal vibrations from lignin, while the peak near ~1710–1730 cm^{-1} corresponds to C═O stretching of carbonyl/ester groups. Additional bands around ~1450–1380 cm^{-1} are linked to C—H bending and aromatic ring vibrations. The strong feature at ~1200–1000 cm^{-1} is attributed to C—O stretching and C-O-C vibrations of alcohol and ether linkages in polysaccharides, while weaker signals near ~1100–1050 cm^{-1} may also include contributions from C—N stretching vibrations. Thermal treatment weakened the O—H band in both C_{opt} and C_{val}, reflecting dehydration, decarboxylation, and devolatilisation, while the relative intensity of aromatic C═C (~1580–1620 cm^{-1}) increases, indicating enhanced aromatic condensation and formation of more thermally stable sp^2 carbon frameworks. Aliphatic C—H bands decrease, confirming progressive aromatisation. Compared to C_{opt}, C_{val} exhibits a weaker C—O fingerprint region intensity (~1200–1000 cm^{-1}), suggesting more extensive removal of oxygen-containing functional groups, whereas the slightly higher residual C—O contribution in C_{opt} indicates that impregnation may stabilise certain oxygenated species or alter carbon restructuring during pyrolysis. The retention of oxygen-containing surface functionalities in Copt may also enhance the reactivity of the carbon matrix toward subsequent CO_2 gasification by providing additional

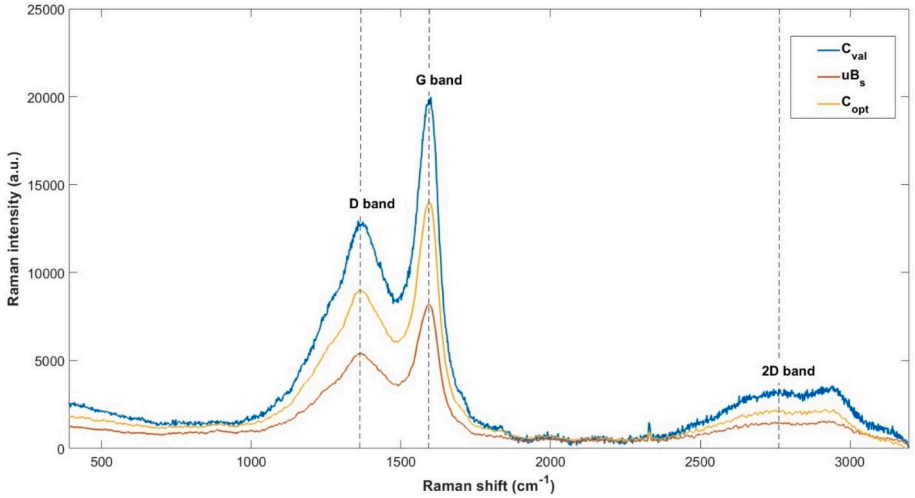

Fig. 9. Raman spectra of uB_s, C_{val} and C_{opt}.

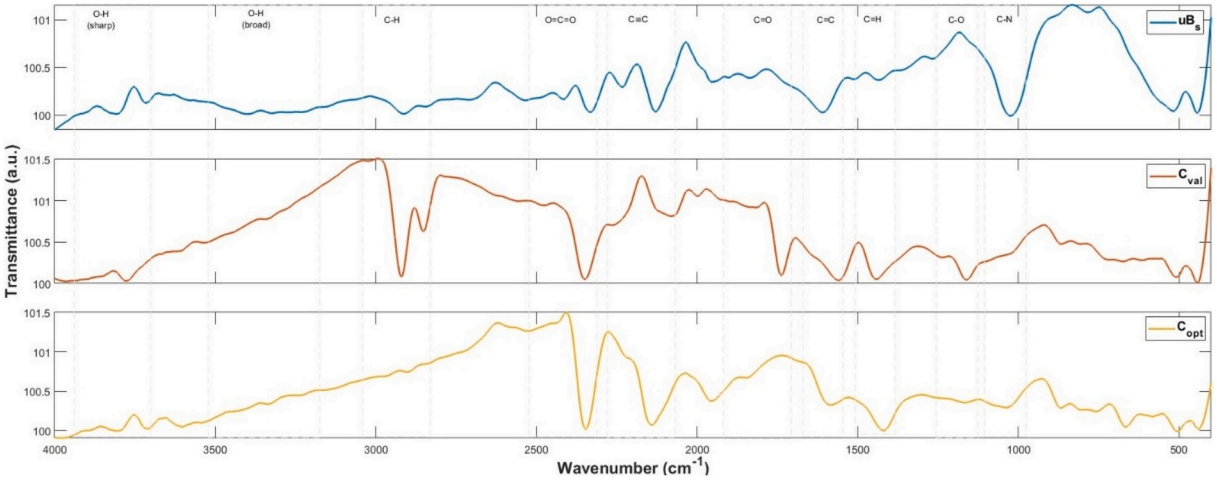

Fig. 10. FTIR spectra of uB_s, C_{val} and C_{opt}.

defect sites for carbon conversion. This observation is consistent with previous studies reporting that calcium species promote devolatilisation, facilitate carbon matrix rearrangement during pyrolysis, and increase the susceptibility of the resulting char to micropore development during physical activation. Overall, the spectra demonstrate conversion from polar, lignocellulosic precursors to predominantly aromatic, condensed carbon frameworks.

3.7. Physical activation of optimum surface-enhanced char

Two activating agents were investigated: CO_2 (diluted with N_2) and steam (cooled with N_2), to further develop porosity and enhance CO_2 adsorption performance of C_{opt}. The activation campaigns were designed to evaluate the effects of temperature, activation time, and activating gas composition or flow rate on the resulting CO_2 uptake capacity. The use of a diluent (N_2) in CO_2 activation and controlled steam flow rates was intended to moderate gasification severity and minimise excessive carbon burn-off. The full experimental data of both campaigns have been included in Tables S8 and S9 in supplementary information A.

3.7.1. CO_2 activation

CO_2 activation of C_{opt} was conducted over a temperature range of 750–950 °C, activation times between 30 and 90 min, and CO_2 concentrations of 50–100 vol% in CO_2/N_2 mixtures with total gas flow as stated in Section 2.5. The results demonstrate that moderate activation severity yields the highest CO_2 uptake capacity, while excessive temperature, time, or CO_2 concentration leads to performance deterioration. At 750–850 °C, CO_2 uptake capacities between 0.83 and 0.87 mmol g^{-1} were achieved under intermediate activation times (60–90 min) and moderate CO_2 concentrations (50–75 vol%). The highest uptake (0.87 mmol g^{-1}) was obtained at 750 °C for 90 min with 75 vol% CO_2, highlighting the importance of controlled gasification in preserving microporosity. Similarly, short activation times at 750 °C (30 min, 75 vol% CO_2) produced high adsorption capacity (0.83 mmol g^{-1}), indicating rapid pore development under milder conditions. In contrast, increasing activation severity resulted in a sharp decline in CO_2 uptake performance. At 950 °C, particularly under longer activation times and higher CO_2 concentrations, CO_2 uptake dropped dramatically to values as low as 0.02–0.25 mmol g^{-1} (i.e. 71–97% drop compared to the highest uptake 0.87 mmol g^{-1} at the lowest temperature level). This behaviour is attributed to excessive carbon gasification, pore widening, and collapse of microporous structures, as well as potential blockage by calcium-rich residues formed at elevated temperatures.

The inclusion of N_2 as a diluent played a critical role in moderating the reactivity of CO_2. Intermediate CO_2 concentrations (50–75 vol%) consistently outperformed 100 vol% CO_2, confirming that dilution suppresses aggressive gasification and promotes the formation of adsorption-relevant micropores. Replicated centre-point runs (850 °C, 60 min, 75 vol% CO_2) showed good reproducibility, further validating the robustness of the experimental design (as seen in Table S8 in supplementary information A). The design response optimisation was identified in Minitab and subsequently validated experimentally. These conditions have been described in Table 9. Overall, CO_2 activation proved effective under mild-to-moderate conditions, with excessive severity leading to structural degradation and loss of adsorption capacity. The inconsistency of the validated response compared to the prediction can be attributed to the low predictive R^2 value of the model (25.92%).

3.7.2. Steam activation

In contrast to CO_2 activation, steam-activated samples generally exhibited significantly lower CO_2 uptake, indicating a fundamentally different interaction between steam and the Ca-enhanced char. The highest CO_2 uptake achieved via steam activation was 0.29 mmol g^{-1}, obtained at 750 °C for 30 min with a steam flow rate of 1.0 g min^{-1}. Moderate performance was also observed at 750 °C and 60–90 min, where CO_2 uptake ranged from 0.10 to 0.18 mmol g^{-1} depending on steam flow rate. These results suggest that lower temperatures favour limited pore development without excessive carbon consumption. However, increasing steam flow rate, temperature, or activation time consistently led to reduced adsorption performance. At 850–950 °C, CO_2 uptake results were typically below 0.06 mmol g^{-1}, regardless of steam flow rate. This behaviour is attributed to the highly aggressive nature of steam activation, which promotes rapid carbon gasification (Eq. (9)), pore coalescence, and loss of microporosity. Centre-point experiments (850 °C, 60 min, 1.0 g min^{-1} steam) showed low but reproducible CO_2 uptake (0.04–0.06 mmol g^{-1}), confirming that steam activation under these conditions does not favour micropore formation in the Ca-enhanced char system.

The design response optimisation was identified in Minitab

Table 9
Response optimisation of CO_2 activation campaign (predicted and validated).

CO_2 uptake Response	Response (mmol g^{-1})	Temperature (°C)	Activation time (minutes)	CO_2 concentration (%)
Predicted	1.05	750	90	0.50
Validated	0.80 ± 0.024	750	90	0.50

Table 10
Response optimisation of steam activation campaigns (predicted and validated).

Design	CO_2 uptake Response	Response Prediction (mmol g^{-1})	Temperature (°C)	Activation time (minutes)	Steam flow rate (g min^{-1})
BBD (750–950 °C)	Predicted	0.26	750	30	0.77
Combined BBD (750–950 °C) and OFAT (450–750 °C)	Predicted	0.84	450	30	0.50
Combined BBD and OFAT	Validated	0.73	450	30	0.50

(Table 10). However, to investigate the effect of lower temperatures on steam activation, OFAT analysis was conducted at the identified optimum activation time and steam flow rate for temperatures 450, 550, 650 and 750 °C. The results obtained showed that the lower the temperature the higher uptake confirming have steam temperatures reduce uptake. This OFAT results were included in the existing BBD design, and the combined design was response optimised yielding a redefined optimum prediction (Table *10*). The initial BBD design had adjusted and predicted R^2 values of 76.98 and 0% respectively. However, after combining the OFAT design to the BBD design, the adjusted and predicted values were 75.04% and 48.15% respectively (confirming better prediction at lower levels). Overall, steam activation was found to be less effective than CO_2 activation for enhancing CO_2 adsorption performance. While limited improvements were observed under mild conditions, steam activation generally resulted in over-activation and degradation of adsorption-relevant pore structures.

The combined results provide direct evidence that controlled CO_2 activation promotes selective micropore development, while excessive activation (e.g. with steam) leads to pore widening, structural collapse, and loss of adsorption-relevant surface area. The optimum activated carbon (AC_{opt}) was determined to be the CO_2 optimum activated carbon identified in Section 3.7.1.

3.8. Characterisation & analysis of optimum activated carbon

The proximate and ultimate analyses of the optimised activated carbon show that activation transformed the C_{opt} into a more developed activated carbon (AC_{opt}) while retaining a similar carbon content (Table *8*). AC_{opt} exhibits a pronounced reduction in hydrogen and volatile matter, indicating enhanced aromatisation and devolatilisation during activation, alongside a slight increase in nitrogen and a small decrease in moisture. Although FC decreased from 69.21 to 61.08 wt% due to partial carbon burn-off associated with pore formation, the most notable change is the substantial rise in ash content (from 10.81 to 23.42 wt% i.e. 116% increase). This increase reflects the relative concentration of inherent mineral matter in AC_{opt} as carbon was selectively gasified during physical activation, a commonly observed effect in physically activated carbons.

N_2 physisorption analysis of AC_{opt} revealed a BET total accessible surface area of 463.38 m^2g^{-1} with linearity established in the BET range 0 to 0.1 with C constant 1878.88 (N_2 isotherm and all data in Supplementary Information B). The developed porous carbons exhibited BET surface areas comparable to those reported for several biomass-derived activated carbons prepared using physical activation. For example, CO_2-activated biomass carbons typically exhibit BET surface areas in the range of approximately 300–800 m^2 g^{-1} depending on precursor type and activation severity, while steam-activated carbons commonly range between 400 and 2000 m^2 g^{-1} [46]. The BET total accessible surface area achieved for AC_{opt} (463.38 m^2 g^{-1}) falls within the lower–middle range reported for physically activated biomass-derived carbons, despite being synthesised exclusively from industrial biomass combustion residues and waste eggshell-derived calcium without chemical activating agents. This demonstrates the effectiveness of the combined calcium-assisted pyrolysis and CO_2 activation strategy for developing porous structures from low-value waste feedstocks. The t-plot analysis found the external surface area to be 92.03 m^2 g^{-1} with linearity established in the relative pressure range 0 to 1. CO_2 physisorption analysis of AC_{opt} revealed substantial enhancement in micropore surface area (384.3 m^2 g^{-1}) and pore volume (0.091 cm^3 g^{-1}) following CO_2 activation under optimised conditions (Table 5). The external surface area for AC_{opt} was higher than the C_{val} which can be explained by the introduction of calcium species that despite blocking mesopores in C_{opt}, which enabled the formation of more pores during activation. The enhanced microporosity observed after calcium modification followed by CO_2 activation can be explained by the complementary roles of the two processes. During pyrolysis, eggshell-derived calcium species are reported to promote devolatilisation and facilitate carbon matrix rearrangement, generating a more reactive char with increased defect density. Subsequent CO_2 activation proceeds through the endothermic gasification reaction (Eq. (2)) whereby carbon atoms at defect sites and pore walls are selectively consumed, leading to the formation and enlargement of micropores. This behaviour further validates that physical activation of carbons can be used to optimise material porosity for applications (like wastewater treatment and carbon capture) where adsorption is governed primarily by narrow micropores (<1 nm). Consequently, the results suggest calcium modification establishes a carbon structure that is more susceptible to controlled CO_2 gasification, while the activation step further develops the pore network, producing carbons with enhanced microporosity and accessible surface area. Although the present study did not directly investigate the catalytic mechanism, the observed structural evolution is consistent with previously reported calcium-assisted activation mechanisms [33,35].

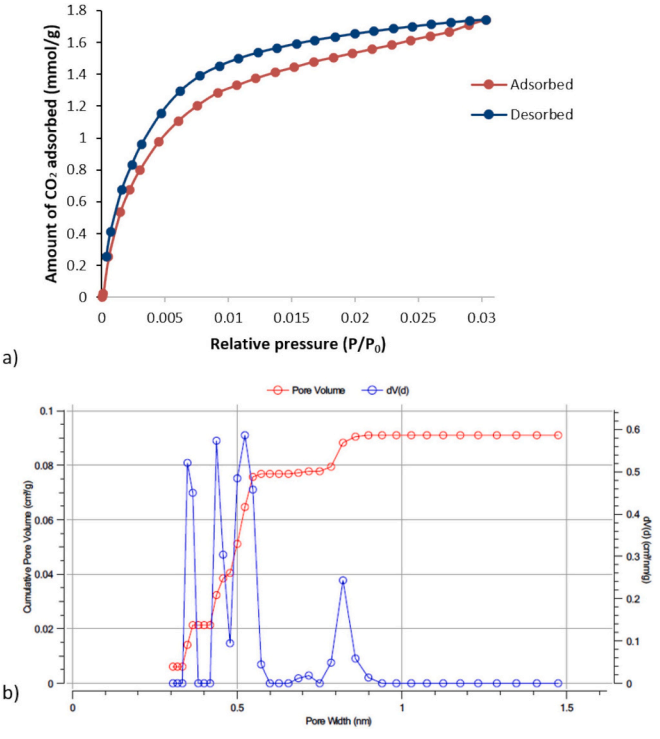

Fig. 11. a) CO_2 adsorption-desorption isotherm and b) pore size distribution for AC_{opt} using NLDFT obtained from physisorption analysis using CO_2 at 273 K.

The CO_2 adsorption isotherm showed a sharp uptake (*Fig. 11*a) at low relative pressures ($P/P_o < 0.1$), confirming the dominance of microporous structures. It is important to note that, although the micropore surface area increases significantly in AC_{opt}, the CO_2 uptake does not scale proportionally (with an increase from 0.64 to 0.87 mmol g^{-1}), indicating that CO_2 adsorption is not governed solely by total micropore surface area. Instead, adsorption is primarily controlled by the accessibility and volume of ultra micropores (< 0.7 nm), which are more sensitive to pore size distribution than total surface area. The total pore volume of AC_{opt} was determined from the N_2 adsorption isotherms at a relative pressure ($P/P_0 \simeq 1$) and was found to be 0.299 $cm^3\ g^{-1}$. The pore size distribution and average mesopore size (2.85 nm) were derived using the NLDFT method based on the N_2 isotherm. In contrast, the average micropore size (0.88 nm) were calculated from CO_2 isotherms using the NLDFT in the pore size range 0.2–1.5 nm (*Fig. 11*b). Additionally, the presence of calcium-containing species may partially obstruct narrow pore entrances or reduce the fraction of accessible adsorption sites, leading to a lower-than-expected increase in CO_2 uptake.

Proximate and ultimate analysis (Table 8) revealed slight decrease in the carbon content which can be explained by the formation of new micropores during activation.

SEM analysis of AC_{opt} showed a morphology comparable to C_{opt}, with a well-preserved carbon framework and evidence of newly developed pore openings (Fig. 12). After CO_2 activation, EDS indicated a similar carbon content (67.4 wt%) but reduced oxygen (21.7 wt%) and increased calcium (9.5 wt%) relative to C_{opt} (Table 6). The enrichment of Ca is attributed to preferential carbon removal during CO_2 gasification (Eq. (2)), which concentrates thermally stable Ca-rich phases in the residual solid. The decrease in oxygen suggests partial decomposition or restructuring of oxygenated surface groups, with remaining oxygen likely associated with stable CaO and $CaCO_3$ species. These results confirm retention and concentration of eggshell-derived calcium after activation, supporting its catalytic role in pore development.

Raman and FTIR were not conducted on the AC_{opt} because the principal chemical and structural transformations were already captured at the modified char stage (C_{opt} and C_{val}). Activation mainly develops porosity and surface area rather than significantly altering the underlying aromatic carbon framework formed during pyrolysis. Since most oxygen-containing functional groups are largely removed prior to activation, additional spectroscopic analysis would provide limited new structural insight. Therefore, molecular fingerprint characterisation focused on the precursor and Ca-enhanced chars, while the activated carbon was evaluated primarily for its textural and adsorption properties.

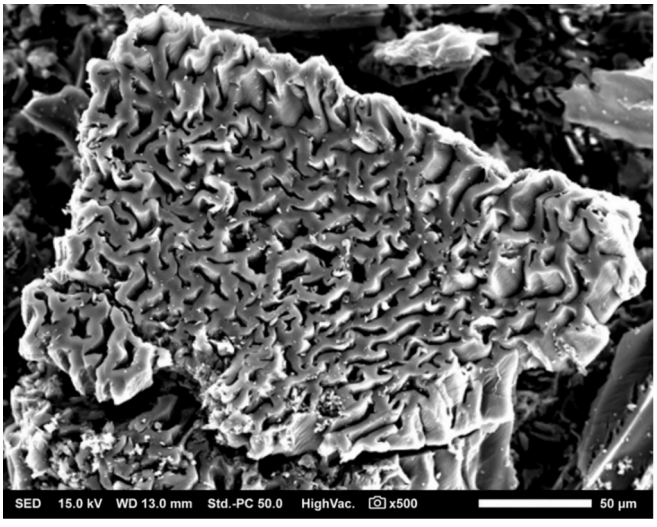

Fig. 12. SEM image of AC_{opt} at x500.

4. Conclusions & future perspectives

Through a comprehensive investigation, this work presents a sustainable strategy for the synthesis of high-performance porous carbon sorbents with the co-valorisation of biomass combustion bottom ash and waste chicken eggshells. By integrating systematic precursor conditioning, statistically optimised pyrolysis, calcium-assisted surface modification, and controlled physical activation, this study demonstrates how heterogeneous waste streams can be transformed into functional materials for various sustainable applications.

Optimised eggshell-free pyrolysis generated a structurally stable baseline char (C_{val}) with high fixed carbon content and improved aromatic ordering, as confirmed by Raman (ID/IG ~ 0.652–0.656) and FTIR analyses showing substantial attenuation of O—H (~3200–3500 cm^{-1}) and C═O (~1730 cm^{-1}) functionalities. Calcium modification influenced carbonisation and pore development, where controlled incorporation by calcium ion impregnation enhanced reactivity and micropore formation, while excessive loading reduced accessible surface area due to pore blockage. CO_2 activation proved more effective than steam, yielding a predominantly microporous structure with a BET accessible surface area of 463 $m^2 g^{-1}$, a micropore surface area of 384 $m^2\ g^{-1}$ (CO_2, 273 K) and an external surface area of 92 $m^2\ g^{-1}$ (N_2, 77 K), highlighting the dominance of narrow micropores critical for adsorption applications. The optimally activated carbon exhibited strong preferential CO_2 adsorption over N_2 under physisorption analysis, and performance governed by micropore architecture rather than total surface area alone. The developed porous carbons exhibited textural properties comparable to those of several physically activated biomass-derived carbons reported in the literature, demonstrating the potential of BCBA and waste eggshells as sustainable precursors for engineered porous materials [46]. Although the combined structural and textural characterisation supports the proposed role of eggshell-derived calcium in promoting pore development, direct determination of calcium speciation before and after activation was beyond the scope of this study. Future investigations employing XPS, together with quantitative phase analysis, could provide further insight into the evolution of calcium species and their catalytic role during carbonisation and activation. Overall, the integration of waste-derived calcium in industrial bottom ash waste during thermal conversion and controlled CO_2 activation provides a scalable, chemically benign pathway for producing efficient carbon sorbents from abundant waste streams, with strong potential for practical applications like soil remediation, wastewater treatment, CO_2 capture and separation of other useful gases.

Current efforts are focused on advancing the synthesised powdered activated carbons toward practical adsorption applications through pelletisation and comprehensive CO_2 capture evaluation. The development of mechanically stable carbon pellets enables assessment of practical adsorption behaviour under fixed-bed conditions, where factors such as pellet strength, diffusional limitations, adsorption capacity, and regeneration performance can be evaluated. The experimentally obtained equilibrium and kinetic adsorption parameters are being incorporated into an experimentally informed one-dimensional dynamic packed-bed model in Aspen Adsorption to assess single-bed temperature swing adsorption (TSA) performance and provide insight into the process feasibility of these waste-derived sorbents.

Further investigations could elucidate the individual contribution of eggshell-derived calcium during the activation process by performing comparative activation studies using both eggshell-free and calcium-modified chars under identical CO_2 activation conditions. While the current study demonstrates that calcium incorporation influences carbon structural evolution during pyrolysis through comparison of eggshell-free and calcium-modified chars, additional controlled activation experiments would enable clearer separation of calcium-assisted pore development from the intrinsic effects of CO_2 activation.

Advanced characterisation techniques, including XPS and high-resolution elemental mapping, could further clarify calcium speciation, dispersion, and interactions with the carbon matrix during thermal treatment. Beyond material-level optimisation, future work could also consider the practical scalability of this waste valorisation approach through process modelling, energy assessment, and techno-economic analysis. Evaluating reactor scale-up, energy requirements associated with thermal conversion and activation, and the production cost relative to conventional activated carbons will be essential to determine the industrial feasibility of BCBA- and eggshell-derived porous carbons. Such assessments, combined with life-cycle and techno-economic analysis, would provide a more comprehensive evaluation of the environmental and economic benefits of converting industrial and food waste streams into value-added adsorbent materials.

CRediT authorship contribution statement

Kofoworola Awodun: Writing – original draft, Visualization, Validation, Methodology, Investigation, Formal analysis, Conceptualization. **Yinghe He:** Writing – review & editing, Supervision, Resources, Project administration. **Salman Masoudi Soltani:** Writing – review & editing, Visualization, Supervision, Resources, Project administration, Methodology, Funding acquisition, Conceptualization.

Declaration of competing interest

We confirm the absence of any competing interests whatsoever in this work.

Data availability

All relevant raw data have been made available in Brunel University of London's repository through Brunel Figshare database at https://doi.org/10.17633/rd.brunel.32648235.

Acknowledgements

SEM-EDS, XRD, and Raman analyses were conducted at the Experimental Techniques Centre (ETC), Brunel University of London, UK, while all other characterisation equipment was housed within the Department of Engineering at Brunel University of London. We would also like to acknowledge Drax power plant, located in Selby, UK, who have been instrumental in this work by supplying actual samples from their biomass combustion boilers. Lastly, we would like to acknowledge our undergraduate interns Dakshan Krishnakumar and Subashini Samraj, who, under authors' direct supervision, helped with the conduction of some basic experiments as part of the summer research internship programme in our lab.

Appendix A. Supplementary data

Supplementary data to this article can be found online at https://doi.org/10.1016/j.fuproc.2026.108554.

Data availability

Research Link Provided

References

[1] W. Tian, H. Zhang, X. Duan, H. Sun, G. Shao, S. Wang, Porous carbons: structure-oriented design and versatile applications, Adv. Funct. Mater. 30 (17) (2020), https://doi.org/10.1002/adfm.201909265. Available from.

[2] L. Wang, Y. Xu, G. Zhai, Y. Zheng, J. Huang, D. Sun, et al., Biophenol-mediated solvent-free synthesis of titanium silicalite-1 to improve the acidity character of framework Ti toward catalysis application, ACS Sustain. Chem. Eng. 8 (32) (2020) 12177–12186. Available from, https://doi.org/10.1021/acssuschemeng.0c03685.

[3] X. Yang, F. Yu, H. Shang, Z. Li, S. Wang, Y. Xing, et al., Comprehensive review of porous particles: Multiscale structure, flow, and transport characteristics, Powder Technol. 453 (2025) 120594.

[4] B. Petrovic, M. Gorbounov, S. Masoudi Soltani, Impact of surface functional groups and their introduction methods on the mechanisms of CO2 adsorption on porous carbonaceous adsorbents, Carbon Capture Sci. Technol. 3 (2022) 100045.

[5] K.M.C. Santos, T.R. Menezes, M.R. Oliveira, T.S.L. Silva, K.S. Santos, V.A. Barros, et al., Natural gas dehydration by adsorption using MOFs and silicas: a review, Sep. Purif. Technol. 276 (2021) 119409.

[6] Y. Song, S. Ma, Pore engineering in metal–organic frameworks and covalent organic frameworks: strategies and applications, Chem. Sci. 16 (26) (2025) 11740–11767.

[7] K. Ahmad, R.U. Sk, F. Shair, M. Kashif, M.A. Nazir, O. Alharbi, et al., Recent advances in covalent organic frameworks for efficient lead ions remediation: insights into adsorption mechanism and environmental potential, Adv. Sustainable Syst. 10 (5) (2026).

[8] F. Khan, K. Ahmad, W. Khan, M. Abdullah, M. Rawal, A.A. Shah, et al., Valorization of banana peel waste into Zr-MOF@AC composite for sustainable methyl orange removal from water with kinetic, isothermal and thermodynamic insights, Desalin. Water Treat. 325 (2026) 101597.

[9] K. Ahmad, M.M.A. Awan, M. Kashif, K. Qureshi, I. Ahmad, M.A. Nazir, et al., MOFs@COFs composites: advances, challenges, and multifunctional applications in emerging technologies, Hybrid Adv. 9 (2025) 100419.

[10] S. Gao, H. Peng, B. Song, J. Zhang, W. Wu, J. Vaughan, et al., Synthesis of zeolites from low-cost feeds and its sustainable environmental applications, J. Environ. Chem. Eng. 11 (1) (2023) 108995.

[11] G. Martínez-Edo, A. Balmori, I. Pontón, A. Martí del Rio, D. Sánchez-García, Functionalized ordered mesoporous silicas (MCM-41): synthesis and applications in catalysis, Catalysts 8 (12) (2018) 617.

[12] S. Chandrasekaran, S. Jadhav, S. Mari Selvam, N. Krishnamoorthy, P. Balasubramanian, Biochar-based materials for sustainable energy applications: a comprehensive review, J. Environ. Chem. Eng. 12 (6) (2024) 114553.

[13] G. Ravindiran, S. Rajamanickam, G. Janardhan, G. Hayder, A. Alagumalai, O. Mahian, et al., Production and modifications of biochar to engineered materials and its application for environmental sustainability: a review, Biochar 6 (1) (2024) 62.

[14] A.H. Asif, L. Shi, T. Ding, S. Zhang, H. Sun, Emerging engineered biochar for environmental and energy applications, J. Bioresour. Bioprod. 10 (1) (2025) 1–3.

[15] I. Correia, M.E. Fernandes, D. Marques-da-Silva, Unveiling the potential of olive oil production residues as adsorbent materials for water treatment: a literature review, J. Bioresour. Bioprod. 10 (4) (2025) 460–475.

[16] Saravanan A, Karishma S, Senthil Kumar P, Rangasamy G. A review on regeneration of biowaste into bio-products and bioenergy: life cycle assessment and circular economy. Fuel 2023 338:127221. Available from: https://linkinghub.elsevier.com/retrieve/pii/S0016236122040455.

[17] K. Lelicińska-Serafin, P. Manczarski, A. Rolewicz-Kalińska, An insight into post-consumer food waste characteristics as the key to an organic recycling method selection in a circular economy, Energies (Basel) 16 (4) (2023) 1735.

[18] Drax Group plc, Drax ESG Performance Report 2024, Available from, www.drax.com/about-us/corporate-governance/compliance-and-policies/, 2024.

[19] Drax Group plc, Drax_Electric_Insights_Report_2025_Q2, 2025.

[20] Waheed M, Yousaf M, Shehzad A, Inam-Ur-Raheem M, Khan MKI, Khan MR, et al. Channelling eggshell waste to valuable and utilizable products: a comprehensive review. Trends Food Sci. Technol. 2020 106:78–90. Available from: https://linkinghub.elsevier.com/retrieve/pii/S0924224420306324.

[21] Z. Kareem, E. Eyiler, Synthesis of hydroxyapatite from eggshells *via* wet chemical precipitation: a review, RSC Adv. 14 (30) (2024) 21439–21452.

[22] M. Baláž, E.V. Boldyreva, D. Rybin, S. Pavlović, D. Rodríguez-Padrón, T. Mudrinić, et al., State-of-the-art of eggshell waste in materials science: recent advances in catalysis, pharmaceutical applications, and mechanochemistry, Front. Bioeng. Biotechnol. 8 (2021).

[23] S. Aditya, J. Stephen, M. Radhakrishnan, Utilization of eggshell waste in calcium-fortified foods and other industrial applications: a review, Trends Food Sci. Technol. 115 (2021) 422–432.

[24] K. Younas, M. Afzaal, F. Saeed, A. Shankar, A. Kumar Bishoyi, N. Khare, et al., A mini-review on egg waste valorization, J. Sci. Food Agric. 105 (5) (2025) 2748–2754.

[25] K. Awodun, Y. He, C. Wu, S. Masoudi Soltani, Catalytic pyrolysis of bio-waste in synthesis of value-added products: a systematic review, Fuel Process. Technol. 275 (2025) 108258.

[26] M. Gorbounov, E. Diaz-Vasseur, D. Danaci, Soltani S. Masoudi, Chemical activation of porous carbon extracted from biomass combustion bottom ash for CO2 adsorption, Carbon Capt. Sci. Technol. 10 (2024) 100151. Available from: https://linkinghub.elsevier.com/retrieve/pii/S2772656823000556.

[27] G. Duan, J. Xiao, Z. Tian, S. Jiang, C. Zhang, K. Liu, et al., Nano-CaCO3 templated porous carbon enable high-rate and ultralong cycle performance supercapacitor, J. Energy Storage 78 (2024) 109934.

[28] N. Díez, M. Sevilla, A.B. Fuertes, Synthesis strategies of templated porous carbons beyond the silica nanocasting technique, Carbon N Y 178 (2021) 451–476.

[29] B. Xu, L. Peng, G. Wang, G. Cao, F. Wu, Easy synthesis of mesoporous carbon using nano-CaCO3 as template, Carbon N Y 48 (8) (2010) 2377–2380.

[30] W. Chen, C. Li, M. Zheng, Y. Li, F. Gong, In situ synthesis of porous SnO2/SnS2@PC anode material with high capacity using calcium carbonate as template for lithium-ion batteries, Materials 18 (21) (2025) 4987.

[31] L. Simão, O.R.K. Montedo, R. Caldato, M.D. de M. Innocentini, M.M. da Silva Paula, E. Angioletto, et al., Porous ceramic structures obtained from calcium carbonate as pore generating agent, Mater. Sci. Forum 775–776 (2014) 755–760.
[32] A. Veses, M. Aznar, I. Martínez, J.D. Martínez, J.M. López, M.V. Navarro, et al., Catalytic pyrolysis of wood biomass in an auger reactor using calcium-based catalysts, Bioresour. Technol. 162 (2014) 250–258. Available from, https://linkinghub.elsevier.com/retrieve/pii/S0960852414004519.
[33] Y. Xu, W. Qu, B. Sun, K. Peng, X. Zhang, J. Xu, et al., Effects of added calcium-based additives on swine manure derived biochar characteristics and heavy metals immobilization, Waste Manag. 123 (2021) 69–79. Available from, https://linkinghub.elsevier.com/retrieve/pii/S0956053X21000313.
[34] H. Li, Y. Wang, N. Zhou, L. Dai, W. Deng, C. Liu, et al., Applications of calcium oxide–based catalysts in biomass pyrolysis/gasification – a review, J. Clean. Prod. 291 (2021) 125826.
[35] Q. Dong, S. Ren, S. Zhang, S. Huang, Y. Guo, H. Li, et al., Role of calcium ion in moso bamboo pyrolysis under microwave irradiation, Fuel Process. Technol. 211 (2021) 106598. Available from, https://linkinghub.elsevier.com/retrieve/pii/S0378382020308894.
[36] American Society for Testing and Materials, Test Method for Ash in Wood. Vol. ASTM D1102-84, ASTM International, West Conshohocken, PA, 2021.
[37] J.F. Strange, P.L. Walker, Carbon-carbon dioxide reaction: Langmuir-Hinshelwood kinetics at intermediate pressures, Carbon N Y 14 (6) (1976) 345–350.
[38] C. Schneider, M. Zeller, D. Böhm, T. Kolb, Influence of pressure on the gasification kinetics of two high-temperature beech wood chars with CO2, H2O and its mixture, Fuel 299 (2021) 120523.
[39] D. Lozano-Castelló, D. Cazorla-Amorós, A. Linares-Solano, Usefulness of CO2 adsorption at 273 K for the characterization of porous carbons, Carbon N Y 42 (7) (2004) 1233–1242.
[40] T. Kan, V. Strezov, T.J. Evans, Lignocellulosic biomass pyrolysis: a review of product properties and effects of pyrolysis parameters, Renew. Sust. Energ. Rev. 57 (2016) 1126–1140. Available from, https://linkinghub.elsevier.com/retrieve/pii/S1364032115015683.
[41] M. Gorbounov, B. Petrovic, S. Ozmen, P. Clough, Soltani S. Masoudi, Activated carbon derived from Biomass combustion bottom ash as solid sorbent for CO2 adsorption, Chem. Eng. Res. Des. 194 (2023) 325–343.
[42] I. Teodorescu, R. Erbaşu, J.M. Branco, D. Tăpuşi, Study in the changes of the moisture content in wood, IOP Conf. Ser. Earth Environ. Sci. 664 (1) (2021) 012017.
[43] L. Segal, J.J. Creely, A.E. Martin, C.M. Conrad, An empirical method for estimating the degree of crystallinity of native cellulose using the X-ray diffractometer, Text. Res. J. 29 (10) (1959) 786–794.
[44] J. Rouquerol, P. Llewellyn, F. Rouquerol, Is the Bet Equation Applicable to Microporous Adsorbents?, 2007, pp. 49–56.
[45] Q. Wang, X. Zhang, S. Sun, Z. Wang, D. Cui, Effect of CaO on pyrolysis products and reaction mechanisms of a corn stover, ACS Omega 5 (18) (2020) 10276–10287.
[46] M.S. Reza, C.S. Yun, S. Afroze, N. Radenahmad, M.S.A. Bakar, R. Saidur, et al., Preparation of activated carbon from biomass and its' applications in water and gas purification, a review, Arab. J. Basic Appl. Sci. 27 (1) (2020) 208–238.